Research Article

Thiocarbamoyl sulfamic acid-derived mesoporous silica: a comprehensive study on selective adsorption of cobalt and lithium from spent lithium-ion batteries

Huda M Younis[*] ⓘ

Abstract

BACKGROUND: The recycling of spent lithium-ion batteries (LIBs) is crucial for resource conservation and environmental sustainability, particularly due to the valuable metals they contain, such as cobalt and lithium. This study focuses on developing an ion-exchange method for cobalt recovery from waste LIB solutions, using a mesoporous silica derivative of carbamoyl sulfamic acid (PST-SA) as the adsorbent.

RESULTS: The batch method for adsorption experiments identified the most effective conditions: a pH of 8, 0.08 g PST-SA, and a shaking time of 60 min, at room temperature. These experiments demonstrated a remarkable cobalt uptake capacity of 270.70 mg g^{-1}, highlighting PST-SA's exceptional adsorption capabilities. Additionally, thermodynamic studies revealed the adsorption process to be both endothermic and spontaneous, enhancing our understanding of its chemically reactive mechanisms.

CONCLUSIONS: The practical application of PST-SA, particularly when processing spent LIBs, showcases its real-world utility. The efficient separation of cobaltous oxalate and lithium phosphate into pure forms emphasizes PST-SA's potential in recycling and resource recovery. Given its cost-effectiveness and strong adsorption capacity, PST-SA stands out as an excellent solution for the removal of Co(II) from discarded LIBs, promoting sustainable material recovery practices.
© 2024 Society of Chemical Industry (SCI).

Supporting information may be found in the online version of this article.

Keywords: adsorption; cobalt; lithium separation; mesoporous silica derivative; spent lithium-ion batteries

INTRODUCTION

The distinctive qualities of lithium-ion batteries, used in electronics, electric vehicles, and various battery technologies, underscore the significance of cobalt and lithium.[1,2] These metals exist in the cathode solution of used lithium-ion batteries (LIBs), necessitating their extraction from the mixture before recycling can commence. Projections indicate that by 2050[3] cobalt consumption in the EU could surpass required levels by up to 15 times,[3] while lithium demand may exceed necessary amounts by up to 60 times.[4] Rapid waste accumulation, fueled by high consumption rates and user negligence, poses environmental challenges. Improper disposal in electronic scrap landfills or waterways can lead to cobalt and lithium leaching issues.[5] Future prospects encompass the sustainable retrieval and recycling of cobalt and lithium from water-based waste streams,[1] aligning with the circular economy concept,[4] which aims to preserve resources and minimize adverse impacts. Given the imperative to establish a low-carbon economy and the role of electric vehicles in this transition,[3] research into battery metals is poised for substantial growth in the coming years, building upon its historical relevance.

Companies have directed efforts toward cobalt extraction from diverse sources, including mines and residues, driven by the escalating demand for this metal, which is primarily used in the production of electric vehicle batteries.[6-13] Botelho Junior *et al.*[14] delved into techniques to retrieve cobalt from the leachate of nickel laterite waste, utilizing methods such as ion exchange and solvent extraction. Additionally, the research focused on hydrometallurgy of cobalt recovery from spent LIBs, involving leaching and solvent extraction.[15] Recycling discarded batteries holds paramount importance for a circular economy, and hydrometallurgy, involving extraction in aqueous media, is preferred for its energy efficiency and selective metal recovery.[16]

LIBs – the greatest prevalent rechargeable batteries – are esteemed for their advantageous properties, including low weight, high thermal stability (ranging from −20 to 60 °C), and numerous charge–discharge cycles. LIBs have become an integral part not only of the automobile industry and large-scale grid energy storage systems but also an array of information technology equipment (ITE) like computers, mobile phones, and other

* Correspondence to: Huda M Younis, College of Dentistry, University of Basrah, Iraq. E-mail: hudamahdi43@yahoo.com; huda.younis@uobasrah.edu.iq

College of Dentistry, University of Basrah, Basrah, Iraq

portable electronic devices. Between 2014 and 2019, the use of LIBs in these movable devices surged significantly, exemplified by the marked increase in specific battery types: 29% of these were Li–Ni–Mn–Co oxide (LNMC) batteries and 37% were Li–Co oxide (LCO) batteries, underscoring the diverse applications and growing reliance on these power sources in various technology sectors.[17-22] Widely utilized in mobile phones, computers, and other information technology and connection devices, LIBs also play a pivotal role in the automotive sector and extensive grid-based energy storage. Between the years 2014 and 2019 the use of LIBs in transportable electronics surged, with LNMC batteries comprising 29% and LCO batteries comprising 37%.[17-22] Valued at an estimated 33.1 billion US dollars, LIBs are a crucial component of portable electronic devices.[23]

Approximately 90% of the economic value in used LIBs is derived from their metal content, particularly in the active cathode. Cobalt, with an anticipated presence of 4500 t in 1200 million mobile battery pieces,[24,25] is considered the most valuable component. The commercial recycling capability for LCO batteries is valued at $8900 per tonne. In contrast, the significantly higher value of cobalt in 2017, at $55 000 USD per tonne of discarded LIBs, suggests that the economic potential for reuse is lucrative in the case of batteries containing cobalt. The economic viability of battery recycling according to numerous parameters, such as the composition of the batteries, market demand for recovered materials, and the efficiency of the recycling processes. Cobalt, being a valuable and critical metal, contributes significantly to the economic feasibility of recycling LIBs.

Designated as a vital, precious, and strategic metal by the European Commission in 2017, cobalt's inflexible manufacturing categorizes it as a potential threat to market supply and demand structures (EU, 2017). Predictions indicate that by 2025[6,26-28] more than half of the global cobalt resources will have been utilized by the LIBs sector.

Pyrometallurgical and hydrometallurgical processes[29,30] have proven effective in extracting cobalt from spent LIBs. Some studies propose recycling LIBs without preliminary breakdown.[31-34] However, both hydrometallurgy and pyrometallurgy have drawbacks, such as the use of excess acids and organic solvents in hydrometallurgy and the necessity for high temperatures in pyrometallurgy.[35,36] Further investigation into the industrial application of LIB recycling for cobalt is essential, as its potential has not been fully realized, and its implementation remains somewhat limited. Presently, the most effective method for metal recovery involves solid-phase extraction, utilizing sorbents with chemically modified surfaces to optimize the process.[37,38]

Simply put, adsorption refers to the process where an adsorbent captures a material (the adsorbate) dispersed within a fluid or gas, facilitated by mass transfer. This method is favored for pollution cleanup because of its straightforwardness and economic efficiency and cost-effectiveness. It employs various adsorbents, including activated carbon, chitosan, bacteria, carbon nanotubes, α-alumina, palygorskite, resins, chitin, soils, and biosorbents such as watermelon rind, rice straw, *Spirulina*, and *Shewanella*, specifically for the elimination of cobalt from water.[39-45]

Bodies of water sediment contain cobalt in both radioactive and non-radioactive forms.[46] Conversely, research into minerals, soils, sediment, and environmental materials reveals that cobalt adsorption depends upon the presence of clay minerals, iron, and manganese oxides, in soils and sediment.[47] Therefore, characterizing the adsorbent and its functional groups is crucial for understanding cobalt's behavior and the potential pathways in the adsorption process.

This study is designed to prepare a novel adsorbent with the ability to adsorb and separate cobalt from its aqueous solutions and spent LIBs. The prepared adsorbent underwent thorough characterization to confirm its composition using various investigative tools. Adsorption conditions, including pH, sorbent dose, reaction time, cobalt concentration, and temperature, were systematically tested to identify the optimal parameters for cobalt adsorption.

MATERIALS AND CHEMICALS

In our examination of secondary market LIBs, the primary cathode component was identified as $LiCoO_2$ (ICR). To obtain the cathode powder, we followed a process involving draining and dismantling used LIBs. The working leaching solution for cobalt and lithium were produced with HCl as acid and H_2O_2 as oxidizing agent, detailed in the Supporting Information. Our supply of HCl 36%, 30% H_2O_2, oxalic acid, and Na_2CO_3 anhydrous type was sourced from Aladdin Chemical Co., Ltd (Shanghai, China). Additionally, isophthalic acid, thiourea, ethyl alcohol, chlorosulfonic acid, and triethoxy(3-isocyanatopropyl)silane (TEOS) were procured from Merck Life Science Co., Ltd (Shanghai, China). The chemicals utilized in our experiments required no further purification as they were all of analytical grade. For the procurement of purified water necessary for our procedures, we utilized a Milli-Q 18.5 M water purification system supplied by Kertone Water Treatment Co., Ltd of China. All reagents used were of analytical grade and required no additional purification before application.

Cobalt solutions

All working solutions were prepared with distilled water and cobalt(II) salt, namely nitrate hexahydrate ($Co(NO_3)_2.6H_2O$) with a purity of 99%. The pH for all cobalt solutions was adjusted to 5.5, except for the pH–adsorption experiments. Cobalt concentration was determined analytically using atomic absorption spectrophotometry (AAS; Varian AA240, Palo Alto, California, United States) with a calibration curve generated from a 1000 mg L^{-1} cobalt reference (Merck). These solutions were cobalt-based aqueous solutions.

Adsorption batchwise

The batch sorption trails were conducted by introducing the solution along with an appropriate dose of a mesoporous silica derivative of carbamoyl sulfamic acid (PST-SA) into a 100 mL Erlenmeyer flask placed in a shaker–incubator apparatus of type FTSH-301 MINI (SP) at 150 rpm. In the initial trial for Co(II) adsorption, 0.1 g L^{-1} PST-SA was used, exploring the pH range of 2–10 with a starting Co(II) concentration of 250 mg L^{-1}. The stirring duration was set at 30 min, and the temperature was preserved at 25 °C to identify the optimal parameters influencing Co(II) adsorption.

For pH adjustments, sodium hydroxide and hydrochloric acid solutions were employed. Another set of tests was conducted to determine the optimal adsorbent dose, dosing from 0.01 to 0.25 g L^{-1}. This series of tests followed standard operational parameters. Kinetic testing conditions included a temperature of 25 °C, 250 mg L^{-1} initial concentration of Co(II), and varying durations from 5 to 120 min.

Initial Co(II) concentrations between 250 and 1500 mg L^{-1} were employed in equilibrium experiments. Sorption kinetics were

used to control the time required to reach equilibrium. Sorbents were evaluated for their ability to uptake Co(II) in the presence of typical associated ions through a series of binary sorption experiments. The final Co(II) concentrations in multicomponent adsorption experiments were investigated using ultraviolet–visible spectroscopy (Ultra-3660 spectrophotometer, RIGOL, Rigol Technologies, Beijing, China) and AAS (Varian AA240). Each experiment was performed in duplicate, and the results shown are the averages.

The calculation of adsorption capacity (q_t (mg g^{-1})) utilized the following mathematical equations, which yielded the following results for the uptake capacity and Co(II) ion adsorption efficiency:

$$q_t = \frac{(C_0 - C_t)V}{m} \tag{1}$$

$$S\% = \frac{C_0 - C_e}{C_0} \tag{2}$$

where q_t represents the quantity of cobalt ions adsorbed per unit mass at time t (mg g^{-1}). The equation parameters are defined as follows: C_o is the cobalt ion initial concentration (mg L^{-1}); C_e is the concentration of cobalt ions at time t or at equilibrium (mg L^{-1}); V represents the volume of aqueous solution of Co(II) ion (L); and m is the amount of working adsorbent (g).

Characterizations studies

Characterization investigations were carried out using various analytical methodologies. The concentrations of dissolved metal ions were determined using inductively coupled plasma optical emission spectroscopy (ICP-OES) with an Optima 7000DV instrument (PerkinElmer, Waltham, MA, USA). Fourier transform infrared (FTIR) spectra were obtained using a Nicolet iS10 spectrophotometer (Thermo Scientific, Waltham, MA, USA).

Additionally, nuclear magnetic resonance (NMR) spectra for ^{1}H (CD4O, 500 MHz) and ^{31}P (CD4O, 202 MHz) of both ionic liquid (IL) and ionic liquid after extraction (IL-ICR) were recorded on a 500 MHz NMR spectrometer (AVANCE III HD 500, Bruker BioSpin GmbH, Ettlingen, Germany). Visual data were captured using an energy-dispersive X-ray spectrometer attached to a field emission scanning electron microscope (S-4800, Hitachi, Tokyo, Japan) equipped with energy-dispersive spectroscopy (EDAX; Genesis XM2, Mahwah, NJ, USA).

Synthesis of carbamoyl sulfamic acid mesoporous silica derivative (PST-SA)

Thionyl chloride was used for the chlorination of isophthalic acid, resulting in isophthaloyl dichloride. The latter was mixed via reflux with a suitable amount of thiourea in ethanol (see Scheme 1) to produce N1,N3-dicarbamothioyl isophthalamide and was then reacted with a suitable amount of TEOS.

N1,N3-dicarbamothioyl isophthalamide (2.4 g) and TEOS (10 g) in a ratio of 1:2 in concentration (mmol) were liquefied in 170 mL dry acetonitrile under a special atmosphere of nitrogen as shown in Scheme 1. For 24 h, the mixture was subjected to heat at 90 °C in a reflux system under inert conditions. Thin-layer chromatography (TLC) was utilized to analyze the results of the reaction. A white precipitate was formed when the solvent was evaporated, and was suspended in dry hexane for 7 h. The white substance was then filtered, washed in hexane, and finally dried in a vacuum. The obtained product was N^1,N^3-bis (((3-(triethoxysilyl)propyl)carbamoyl)carbamothioyl)isophthalamide and named PST.

The materials were synthesized using PST as the source of bridging organic groups and Pluronic P-123 as both the template and structure-directing agent. First, P-123 is dissolved in HCl and water at 45 °C while the mixture is vigorously stirred. The mixture is stirred for 12 h at the specified temperature until a yellowish-white precipitate forms, followed by an additional 12 h of stirring at 90 °C to homogenize the mixture. The resulting yellowish-white precipitate is then separated using filtration, rinsed multiple times with water, and air-dried.

The produced PST was washed in an HCl–ethanol solution for 12 h at room temperature; this procedure was repeated twice to confirm that all traces of surfactant had been removed. The final product (PST) was made by filtering the substance, washing it with C$_2$H$_5$OH, and drying it at 60 °C for overnight.

Finally, after 2 h of stirring at 45 °C, 4 g PST was submerged in chloroform and the mixture was treated with 0.08 mL chlorosulfonic acid (ClSO$_3$H), followed by 18 h of stirring at the same temperature and with the addition of a sufficient quantity of triethylamine to neutralize the hydrochloric acid that had been liberated (see Scheme 1). The final product, designated PST-SA, was an organic–inorganic hybrid mesoporous silica material enhanced by the group of a sulfonic acid that was created by filtering, washing with excess chloroform, and drying in a vacuum.

CHARACTERIZATION OF PST-SA, CHELATING LIGAND

FTIR analysis for products

FTIR analysis data for the PST adsorbent indicates the presence of specific peaks as follows: for stretching vibration of the OH group, the peak appears at 3410 cm^{-1}. Major representative peaks at 3239 cm^{-1} are attributed to stretching vibrations in the —NH group, even though those at 3069 cm^{-1} and in the range 2900–3000 cm^{-1} are the result of aromatic and aliphatic C—H stretching respectively. Two peaks, at 1655 and 1596 cm^1, identify the C=O and C—N groups. Three bands, at 1073, 792, and 457 cm^{-1} of Si—O—Si, are identified as belonging to silica. In addition, Si—O is attributed to a peak at 949 cm^{-1} as seen in Fig. 1.[48-51]

Contrastingly, the FTIR spectrum of PST-SA reveals the disappearance of amino group peaks, accompanied by the emergence of new peaks at specific wavenumbers. Notably, peaks are observed at 1059 cm^{-1}, attributed to the SO$_3$ stretch[52], 1598.86 cm^{-1} for the N—C stretching vibration, 744 cm^{-1} for asymmetric as well as symmetric (C=S) stretching vibrations,[53] 3408.86 cm^{-1} for the OH stretching vibration, and 964 cm^{-1} for the quaternary nitrogen (quaternary ammonium salt (NC$_4$)) asymmetrical stretching.[54] These findings provide conclusive evidence that the PST-SA adsorbent has indeed been successfully manufactured.

Brunauer–Emmett–Teller (BET) surface area of PST and PST-SA

The BET surface areas of the PST-SA material increase with sulfonation branching and are presented in Table 1. The introduction of the sulfonyl group led to a rise in surface area, whereas the pore volume showed an insignificant reduction of the microporous fraction. Supporting Information Fig. SI.1 shows the pore size distributions that correlate with the nitrogen adsorption–desorption isotherms for PST and PST-SA.

There was a unanimous agreement regarding the type IV isotherm for nitrogen adsorption–desorption (according to IUPAC nomenclature).[55] Supporting Information Fig. SI.1 shows that the nitrogen sorption isotherm for PST exhibits an H1-type hysteresis
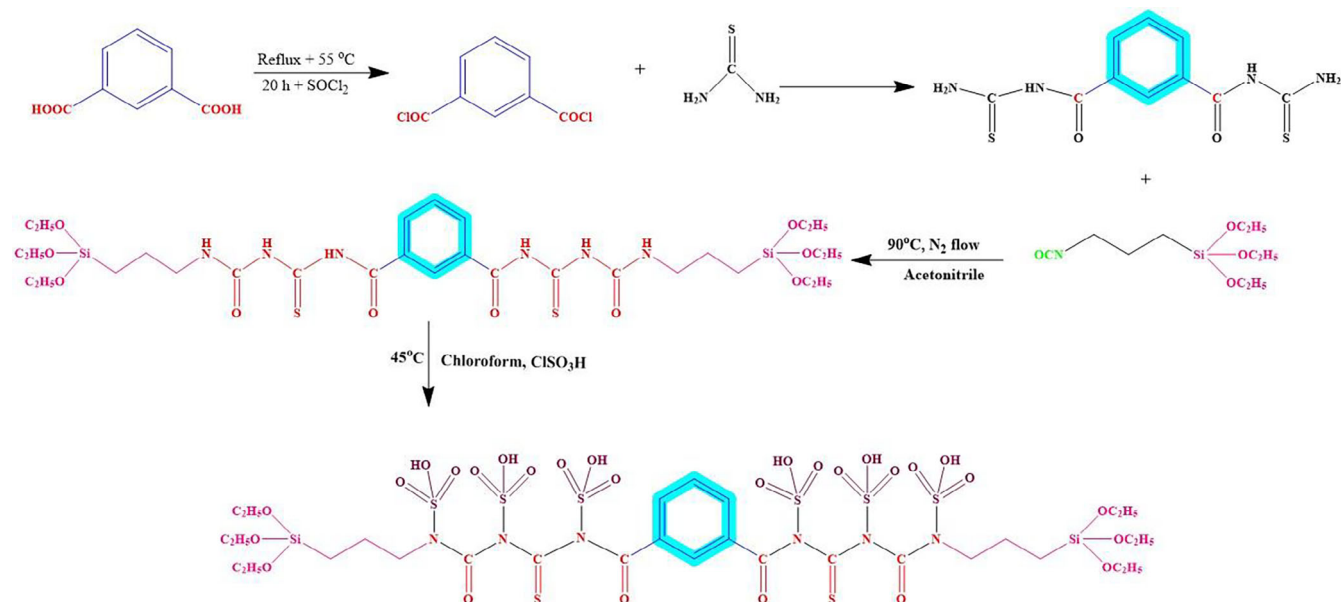
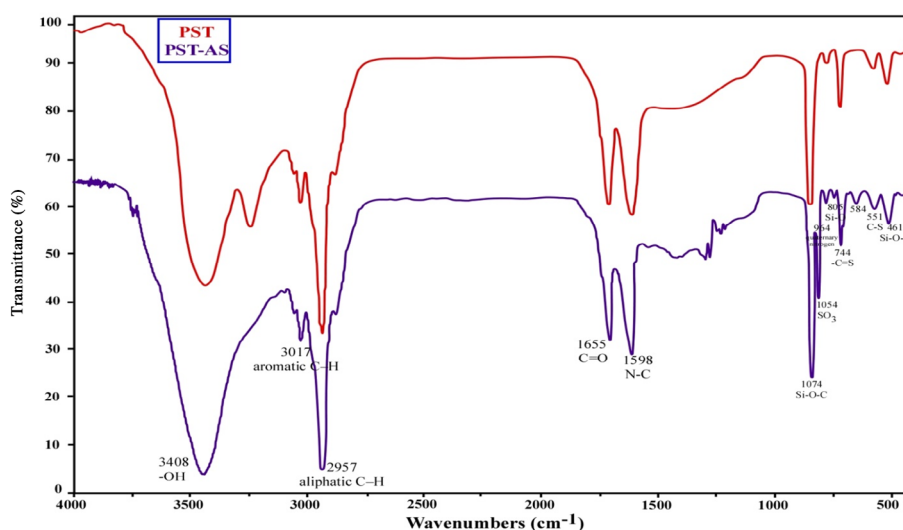**Scheme 1.** Functionalization of PST and PST-SA with chlorosulfonic acid.

Figure 1. FTIR spectrum of PST and PST-SA.

Table 1. PST and PST-SA characteristics; pore size and surface area

Parameter	PST	PST-SA
BET surface area (m² g⁻¹)	456	668
BJH pore volume (cm³ g⁻¹)ᵃ	0.96	0.57
Pore diameter (nm)ᵃ	5.85	5.13
Micropore volume (cm³ g⁻¹)ᵇ	0.103	0.076
Micropore area (m² g⁻¹)ᵇ	206	143

ᵃ Determined from the desorption branch of the N₂ isotherm.
ᵇ Determined from the *t*-plot method (de Boer method).

loop in the pressure ratio ranging from 0.61 to 0.77, while the nitrogen sorption isotherm for PST-SA displays an H^1-type hysteresis loop within the relative pressure range of 0.46–0.73.[56]

^{1}H-NMR analysis

^{1}H-NMR (400.15 MHz, with diluent of DMSO-d$_6$, temp.; 25 °C, TMS) δ, ppm: 7.94 (d, J = 8.3 Hz, 2H, benzene ring), 8.36 (s, J = 2.1 Hz, 1H, benzene ring), 0.72 (t, J = 9.3 Hz, 4H, —CH$_2$ adjacent to silicon atom), 1.79–3.8 (m, 20H, —CH$_2$ aliphatic), 1.21 (t, J = 7.5 Hz, 18H, —CH$_3$ groups), 9.08–9.33 (s, 6H, —OH groups).

For the purpose of determining the structure of a newly synthesized compound, ^{1}H-NMR examination at 400.15 MHz in DMSO-d$_6$ as a working diluent is a powerful and useful tool. Chief δ (ppm) assignments occur in the 7.94–8.36 ppm range, which are associated with the —CH protons of the benzene ring. Multiple assignments to the —CH of benzene rings have been postulated, with each being related to the orientation, proximity, and distance from the primary active sites, which in turn determine the chemical shift and coupling constant values. The significant dissimilarity in proton assignments for —CH$_2$ (δ = 0.72–3.8 ppm) was

found and is believed to be influenced by orientation, proximity, and distance from the principal active sites. At 1.21 ppm, the assignment of methyl groups is considered to be a triplet. Hydroxyl groups, which show up as single, have a greater chemical shift (more de-shielded protons) at 9.08–9.33 ppm. Supporting Information Fig. SI.2 illustrates the use of ^{1}H-NMR in characterizing the PST-SA ligand.

Thermogravimetric analysis of PST-SA adsorbent

Figure 2 shows the thermogravimetric analysis (TGA). Weight loss in the TGA curve between 25 and 150 °C could be the result of the desorption of organic groups and the release of water, solvent, and other adsorbed species of physical type from the outer surface of the PST-SA adsorbent. Decomposition of the grafted thiocarbamoyl sulfumic acid moiety causes a second loss of mass between 150 and 350 °C. Between 375 and 600 °C, silanol groups (Si—OH) are converted to siloxane (Si—O—Si) bridges, which results in a third weight loss.[57,58]

^{13}C-NMR analysis of PST-SA adsorbent

^{13}C-NMR (DMSO-d$_6$, 25 °C, TMS, 100.04 MHz) δ, ppm: 132.8 (s, 4CH, benzene ring), 133.2 (s, 2C, benzene ring), 147.2–163.1 (s, 4C, —C=O groups), 178.1 (s, 2C, —C=S groups), 9.5–58.3 (s, 12CH$_2$), 18.3 (s, 6CH$_3$).

^{13}C-NMR investigation with energy at 100.04 MHz and a diluent of DMSO-d$_6$ is a vital tool that provides very useful information regarding the sum of carbon atoms present in the created compound. The principal δ (ppm) is about 9.5–58.3 and 18.3 ppm, which are connected to methylene and methyl groups, respectively. The —CH$_3$ carbon assignments were established to be more shielded than the other —CH$_2$ carbons because methyl groups were placed at the end of the ethyl group. The deprotonated carbon identification assignment was recognized to be extra de-shielded than methyl and methylene groups, which appeared at 42 ppm. The higher de-shielded carbons of the C$_6$H$_6$ring were also detected at a high chemical shift between 132.8 and 133.2 ppm, which are connected to —CH and —C atoms. It was found that the carbon of thione groups (—C=S, 178.1 ppm), was more de-shielded than the carbonyl group (—C=O, 147.2–163.1 ppm), as the thione group was less polarized than the carbonyl group. The description of PST-SA ligand utilizing ^{13}C-NMR is given in Supporting Information Fig. SI.3.
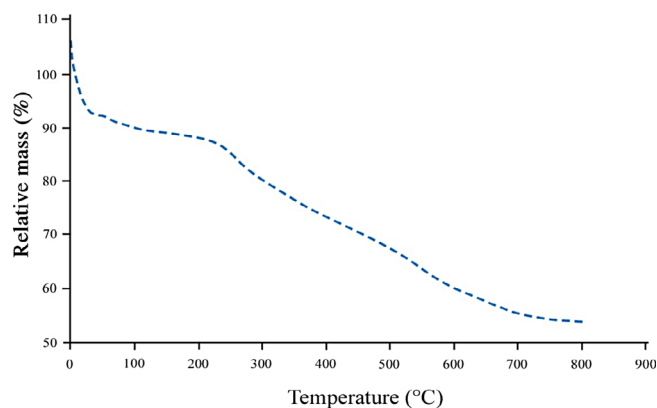

Figure 2. TGA of the PST-SA materials.

Gas chromatographic–mass spectrometric (GC-MS) analysis of PST-SA adsorbent

GC-MS (EI, 70 eV), m/z (% rel.): $[m/z]^+$ of 78, 81, 42, 163, 177, 205, 134, 76, 45, 46 and 164. Anal. Calc. for C$_{30}$H$_{52}$N$_6$O$_{28}$S$_8$Si$_2$ (1257.41 g mol^{-1}): C, 28.66; H, 4.17; O, 35.63; S, 20.4; N, 6.68; Si, 4.47. Found: C, 28.51; H, 4.22; O, 35.71; S, 20.35; N, 6.71; Si, 4.5.

A gas chromatograph connected to a mass spectrometer can be used to make predictions about the purity, molecular structure, and the more stable fragment $[m/z]^+$. GC-MS is also a potent and influential instrument. There is no appearance in the fragmentation pattern of the molecular ion peak that would indicate the molecular weight (MW)of the produced ligand. This disappearance may be due to the high energy used in the electrical impact technique (EI-MS), which is categorized as a hard ionization technique, causing an extensive fragmentation. Some important patterns of fragmentation associated with the prepared ligand were detected – for example, [C$_6$H$_6$]$^\cdot$ with an MWof 78 (C$_6$H$_6$ ring); [SO$_3$H]$^\cdot$ with an MW of 81 (sulfonic acid group); [C$_3$H$_7$]$^\cdot$ with an MW of 42, which is related to the n-propyl moiety; [C$_6$H$_{15}$O$_3$Si]$^\cdot$ with an MW of 163 (triethyl silyl moiety); [C$_7$H$_{17}$O$_3$Si]$^\cdot$ with an MW of 177 (methyl triethyl silyl moiety); [C$_9$H$_{21}$O$_3$Si]$^\cdot$ with an MW of 205 (propyl triethyl silyl moiety); [C$_6$H$_{16}$O$_3$Si]$^\cdot$ with an MW of 164 (triethyl silane moiety); [C$_8$H$_6$O$_2$]$^\cdot$ with an MW of 134 (phthaldehyde moiety); [CH$_4$N$_2$S$_4$]$^\cdot$ with an MW of 76 (thiourea); [C$_2$H$_5$O]$^\cdot$ with an MW of 45 (ethoxide moiety) and MW of 46 defining the formation of [C$_2$H$_5$OH]$^\cdot$ ethyl alcohol moiety. Complete analysis ensures successful PST-SA ligand synthesis. Supporting Information Fig. SI.4 shows an example of PST-SA ligand specification using GC-MS.

Factors controlling the adsorption process

pH study

The study on pH variation reveals a fundamental impact on the adsorption behavior of Co(II) by PST-SA within the pH range 2.0–10 (Fig. 3(A)). The adsorption percentage of Co(II) demonstrated a gradual increase with rising pH, reaching a maximum at pH 8, after which it began to decline. This trend might be attributed to the reduced occupation of protons from acidic media on the adsorption sites of PST-SA, leading to a decrease in its coordination ability with Co^{2+}.

Figure 3(B) illustrates the predominant cobalt(II) species at pH 2–10, including Co(OH)$^+$,Co(OH)$^{3-}$, Co(OH)$_2$, and Co^{2+}, with Co^{2+} being the prevailing species. The sorption reaction primarily targets Co^{2+} at pH $\leq$ 8.4. Notably, the PST-SA adsorbent exhibits exceptional adsorption capacity for Co^{2+} at pH 8.4, where the decreased group protonation allows the non-protonated groups to chelate additional cobalt ions Co^{2+}.

With an increase in pH, the potential of the adsorbent surface becomes increasingly negative, leading to a more robust adsorption of cobalt ions. Remarkably, near-complete elimination of cobalt ions from the solution is observed at pH 8.

The adsorbents exhibit minimal adsorption of cobalt ions under acidic or neutral conditions. However, a noteworthy escalation in adsorption capacity occurs when the pH is $\geq$8. This phenomenon is ascribed to alterations in potential on the surface of the sorbent, as illustrated in Fig. 3(C). Below the point of zero charge (pH$_{zpc}$), the PST-SA surface adopts a cationic charge due to protonation. Conversely, when the solution pH surpasses pH$_{zpc}$, the surface acquires a (−) charge, facilitating cationic ion adsorption.
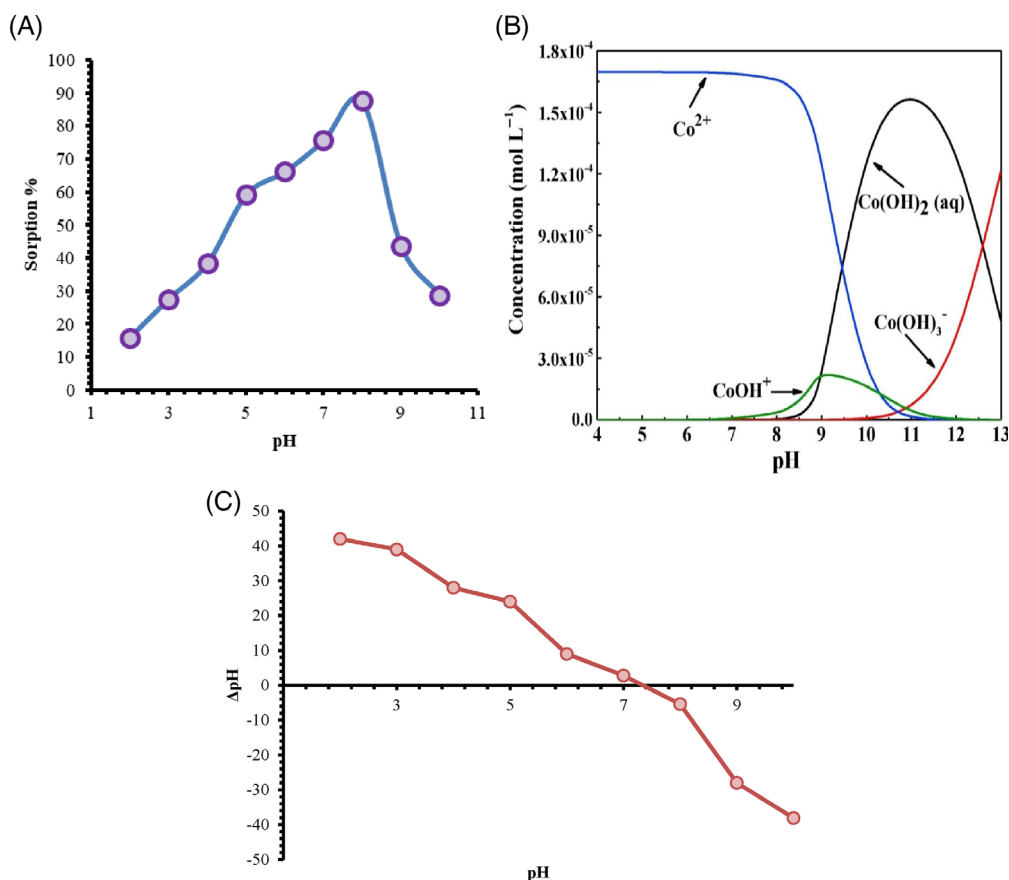
(A)

(B)

(C)

Figure 3. (A) Influence of pH on the elimination of cobalt by PST-SA. Initial cobalt concentration: 250 mg L^{-1}; PST-SA: 0.1 g 20 mL^{-1}; agitation time: 30 min. (B) Mean species of Co^{2+} at different pH values (C_{Co2+} = 1 mol L^{-1}).(C) pH point of zero charges of PST-SA.

Effect of PST-SA dose

Cobalt removal was assessed under constant conditions, including a starting concentration of 250 mg L^{-1} metal, a contact period of 30 min, pH maintained at 8, and an ambient temperature of 25 ± 2 °C. The data, illustrated in Fig. 4(A), indicate that cobalt adsorption improved from 27.4% at a sorbent concentration of 0.01 g 20 mL^{-1} to 87.5% at 0.08 g 20 mL^{-1} in the study. This observed trend aligns with expectations, as the number of adsorbent sites rises proportionally with the dose of sorbent, allowing for more ions to bind to their surfaces.[59] Interestingly, the adsorption of cobalt remained at 87.5% even with an increase in the dosage of PST-SA beyond 0.08 g. This indicates that the quantitative sufficiency of cobalt adsorption was achieved with only 0.08 g PST-SA.

Adsorption time

A critical indicator of an adsorbent's effectiveness is the time necessary to achieve adsorption equilibrium. Experiments were conducted at a starting Co(II) ion concentration (C_o) of 250 mg L^{-1} to evaluate the impact of reaction time on uptake. As illustrated in Fig. 4(B), the adsorption capacity for cobalt ions increases with time. After a relatively slow initial 30 min, the adsorption process accelerates significantly, reaching equilibrium after 60 min. To gain insight into the uptake mechanism, the attained data were fitted using both the pseudo-first-order kinetic model, determined using Eqn (3), and the pseudo-second-order kinetic model, determined using Eqn (4). These models were employed to elucidate the dynamics of the uptake process.

Sorption kinetics

The kinetics of sorption is crucial, as it elucidates the rate at which solutes adhere to surfaces and the chemical processes involved. This knowledge is indispensable for comprehending and optimizing the adsorption mechanism. Since it reveals crucial details about the solute adsorption rate and reaction pathways, adsorption kinetics is a critical part of the sorption process.[60] A kinetics investigation of the sorption process, illustrated in Fig. 4(C), examined how much time was spent in contact with the PST-SA before any significant adsorption of cobalt(II) occurred. It was found that practically all of the cobalt content was adsorbed in the first 60 min. To learn more about the adsorption progression mechanism, the researchers examined three models: the pseudo-first-order (Eqn (3)), pseudo-second-order (Eqn (4)), and intraparticle diffusion (Eqn (5)) models[61,62]:

$$\log(q_e - q_t) = \log q_e - k_1 t/2.303 \tag{3}$$

$$\frac{t}{q_t} = \frac{1}{k_2 q_e^2} + \frac{t}{q_e} \tag{4}$$

$$q_t = k_{int} t^{0.5} + C \tag{5}$$

The equilibrium uptake capability of metal ions is signified by q_e (mg g^{-1}), and the sorption capacity at a specific time t (min) is similarly quantified. The rate constants for the kinetic models – pseudo-first-order, second-order, and intraparticle diffusion – are represented by k_1 (min^{-1}), k_2 (g mg^{-1} min^{-1}), and k_{int}, respectively. Moreover, the constant C (mg g^{-1})

symbolizes the constraint imposed by the thickness of the boundary layer.

Table 2 presents the adsorption rate constants and linear regression correlation coefficients (R^2) for PST-SA. The uptake process of Co(II) on PST-SA material is most accurately described by the pseudo-second-order model, as evidenced by the high correlation coefficient of 0.9945.

To delve deeper into the adsorption mechanisms, we also applied the intraparticle diffusion model (Eqn (6)) to fit the adsorption data. The resulting intraparticle diffusion kinetic plots are illustrated in Supporting Information Fig. SI. 5. It is evident from these plots that the adsorption of Co^{2+} occurred in multiple steps, suggesting that the intraparticle diffusion model does not solely dictate the rate-controlling step in the sorption mechanism.
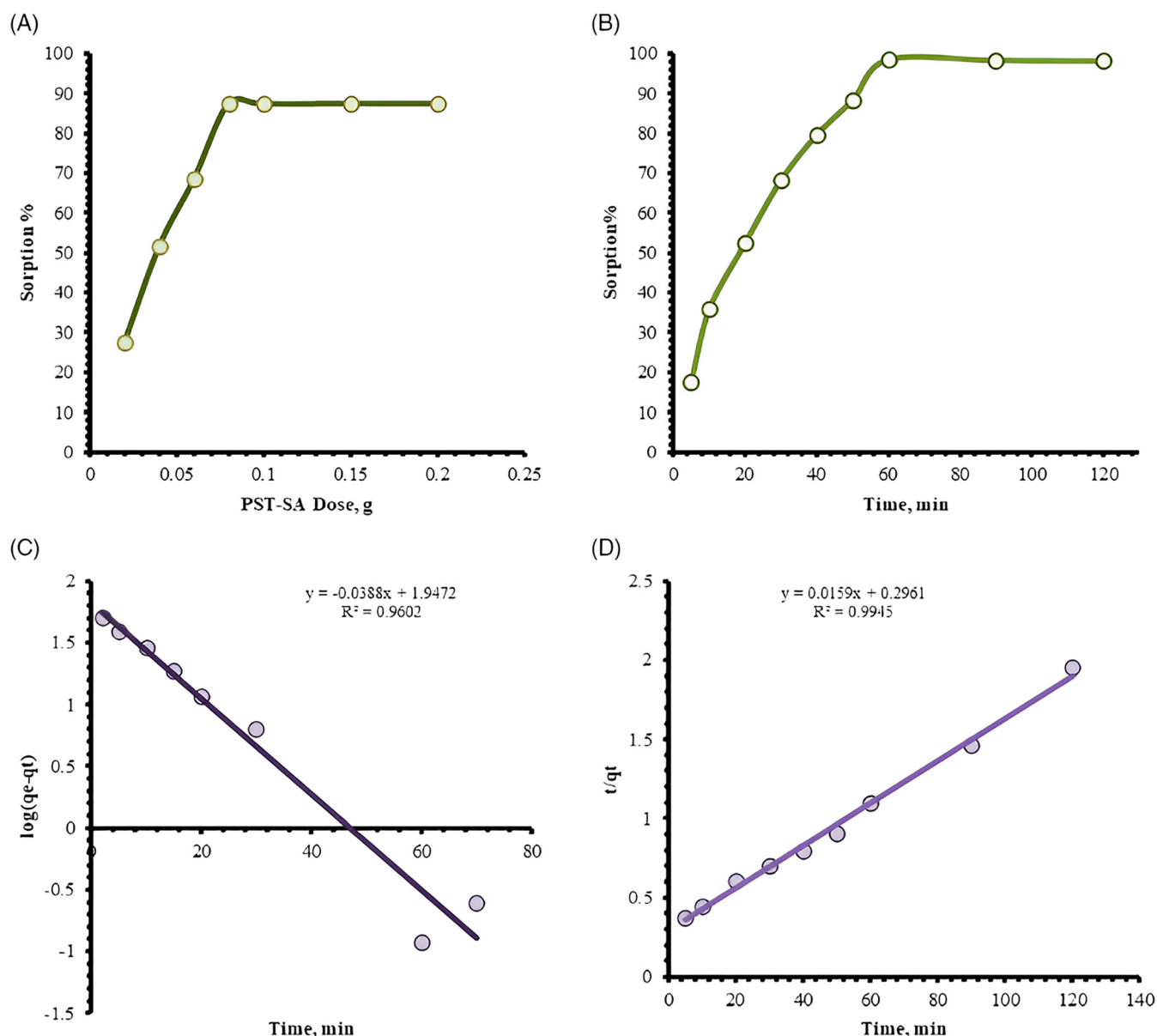

Figure 4. (A) Influence of PST-SA dosage. (B) Influence of contact time. (C) First-order and (D) second-order kinetics on the adsorption process of cobalt. Initial cobalt concentration: 250 mg L^{-1}; pH = 8; contact time: 30 min. (C_0 = 250 mg L^{-1}, pH = 8, V = 20 mL, T = 298 K, and m = 0.08 g).

Table 2. Kinetic factors controlling Co(II) adsorption on PST-SA

First-order kinetics			$q_{max(exp)}$	Second-order kinetics			Intra-particle diffusion model		
K_1	$q_{(max)cal}$	R^2	61.56	K_2	$q_{(max)cal}$	R^2	K_{id}	C_i	R^2
0.0894	88.552	0.9602		0.00085	62.893	0.9945	6.0689	5.8835	0.8672

Additionally, the low R^2 values and intercepts associated with the intraparticle diffusion model indicate a significant boundary layer effect. The positive intercept values further imply rapid adsorption.

$$q_t = k_i t^{1/2} + C_i \tag{6}$$

where q_t (mg g^{-1}) is the amount of adsorbate sorbed at time t. C_i is the intercept and k_i is the intraparticle diffusion rate constant (mg g^{-1} min$^{-1/2}$).

Impact of initial concentration

The sorption of metal ions upon PST-SA is a function of the original Co(II) concentration from 0 to 60 mg L^{-1}. According to the results, the sorption capacity improves as the initial cobalt content in the solution rises, as illustrated in Fig. 5.

Despite the empirical nature of the Freundlich isotherm, it has proven to be a valuable tool for describing sorption processes characterized by intricate interactions between surface-binding sites and the sorbate. Additionally, it can serve as a representation of scenarios where sorbate molecules, once bound, interact with each other. This interaction may be attributed to factors such as hydrophobic effects or the formation of multilayers.[63] Data on sorption were analyzed using a linearized version of the Freundlich sorption isotherm, as shown below. In a mathematical expression, the Langmuir model can be signified as follows (Eqn (7)):

$$q_e = \frac{Q_0 b C_e}{(1 + b C_e)} \tag{7}$$

where q_e is the concentration of the adsorbate at equilibrium (mg g^{-1}). At equilibrium, C_e is the concentration of the Co(II) solution (mg m^{-3}), presented as the concentration of Co(II) solution (mg dm^{-3}) at equilibrium. The constant theoretical or predicted capacity for monolayer adsorption (mg g^{-1}) is shown by Q_o. The energy of adsorption (dm^3 mg^{-1}), is shown by b.

The Langmuir equation can be represented linearly by Eqn (8)[63]:

$$\frac{C_e}{q_e} = \frac{C_e}{q_m} + \frac{1}{q_m K_l} \tag{8}$$

The linear plot of C_e/q_e versus C_e (Supporting Information Fig. SI.6A) was used to calculate the Langmuir constants Q_o and K_l, which were
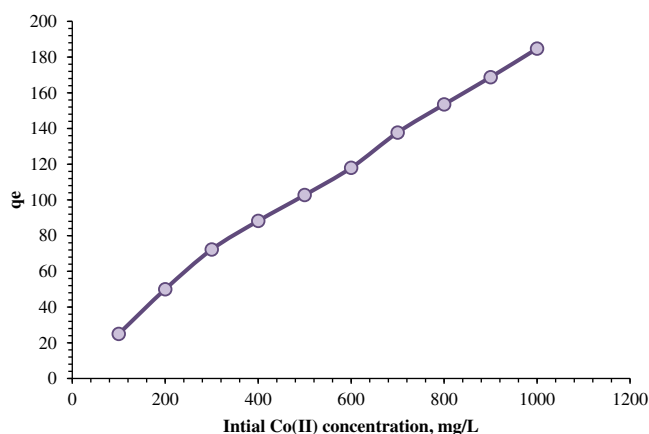
determined to be 212.77 mg g^{-1} and 0.0186 dm^3 mg^{-1}, respectively, according to Table 3.

The intrinsic attributes of the Langmuir isotherm are encapsulated by a dimensionless constant, termed the equilibrium parameter R_L (Eqn (9)), which provides a fundamental description of its nature:[64]

$$R_L = \frac{1}{(1 + b C_0)} \tag{9}$$

where b represents the Langmuir constant and C_0 is presented the initial concentration (mg g^{-1}). The R_L values serve as indicators of the isotherm type, with values ranging from 0 to 1 signifying favorable adsorption conditions. Specifically, for the concentrations of Co(II) examined, the R_L values were determined to lie within the range 0.051–0.177, reaffirming the favorable nature of the adsorption. the adsorption's favorable nature.

The Freundlich isotherm model is signified by (Eqns (10) and (11))[65]:

$$q_e = k_f \log C_e^{1/n} \tag{10}$$

in logarithmic form:

$$\log q_e = \log k_f + \frac{1}{n} \log C_e \tag{11}$$

where the sorption capacity and intensity are quantified by the constants k_f and n, respectively. These constants, integral to the Freundlich isotherm model, are detailed in Table 3. They were deduced from the linear relationship evident in the plot of log q_e against log C_e, as showcased in (Supporting Information Fig. SI.6B). The constants k_f and n specifically characterize the sorption of Co(II) by PST-SA, offering insights into its adsorptive behavior.

The Dubinin–Radushkevich (D-R) isotherm

$$q_e = q_m e^{-B\varepsilon^2} \tag{12}$$

Figure 5. Influence of initial Co(II) concentration on cobalt ion sorption upon PST-SA.

Table 3. Isotherm factors of different models for sorption of Co(II) ions by PST-SA

Kinetic model	Parameter	
Langmuir isotherm	Equation	$y = 0.0037x + 0.2533$
	q_{max} (mg g^{-1})	270.27
	K_1	0.0186
	R^2	0.9919
Freundlich isotherm	Equation	$y = 0.3259x + 1.4815$
	K_f (mg g^{-1})	30.304
	$1/n$ (mg min^{-1} g^{-1})	0.3259
	R^2	0.9483
D-R isotherm	Equation	$y = -0.0078x + 5.5904$
	q_D (mg g^{-1})	267.843
	B_D (mo1^2 kJ^{-2})	0.0078
	E_D (kJ mo1^{-1})	8.01
	R^2	0.9609
Practical capacity	q_{exp}	267.75

The D-R isotherm can be represented in linear form (Eqns (12) and (13)),[66] capturing the essence of adsorption dynamics.

$$\ln q_m = \ln q_m - B\varepsilon^2 \qquad (13)$$

In this model, q_m symbolizes the theoretical saturation capacity (mol g^{-1}), while B denotes a constant reflecting the mean free energy of sorption per mole of the adsorbate (mol^2 J^{-2}). Moreover, the Polanyi potential, represented by ε (Eqn (14)), is intricately linked to the equilibrium concentration as follows:

$$\varepsilon = RT \ln\left(1 + \frac{1}{C_e}\right) \qquad (14)$$

The latter can be described by the universal gas constant R (8.314 J mol^{-1} K^{-1}), the equilibrium concentration of the adsorbate in the solution C_e (mol L^{-1}), and the absolute temperature T (K).

The D-R constants q_m and β are derived from the linear relationship of $\ln q_e$ versus ε^2 and their values are cataloged in Table 3. The constant β facilitates the determination of the mean free energy E (kJ mol^{-1}) of adsorption per adsorbate molecule, which is indicative of the adsorption's nature when it transitions from the solution phase to the solid surface, and can be obtained by calculating the constant using the following relationship:

$$E_D = \frac{1}{(2\beta)^{1/2}} \qquad (15)$$

This value is pivotal in discerning the nature of the adsorption process physical or ion exchange Specifically, an energy barrier (E_D) (Eqn (15)) ranging from 8 to 16 kJ mol^{-1} signals an ion-exchange adsorption mechanism, whereas a value less than 8 kJ mol^{-1} suggests a physical sorption process.[67,68] As depicted in Supporting Information Fig. SI. 6C, the calculated average free energy of sorption for the current study is 8.01 kJ mol^{-1}, aligning closely with the characteristics of an ion-exchange adsorption method.

The experimental uptake closely aligns with the theoretical values, affirming the suitability of the Langmuir model for elucidating the adsorption equilibrium of PST-SA. The high correlation coefficient value ($R^2 > 0.99$) underscores that the Langmuir model offers the finest fit for the results obtained in this investigation.

For Co(II) ions, the correlation coefficient (R^2) is 0.9609, and the sorption energy dissipation (E_D) value is 8.01 kJ mol^{-1}. These findings suggest that the sorption process involves chemisorption followed by ion exchange. Consequently, the sorption mechanism of Co(II) ions on the PST-SA compound can be aptly described by the D-R isotherm, supporting and complementing the results derived from the Langmuir isotherm.

Effect of adsorption temperature

In the uptake temperature study of Co(II) using PST-SA, the addition of 0.08 g (dry mass) of PST-SA to a 1000 ppm Co(II) solution at pH 8 resulted in the following outcomes. The temperature was systematically raised to 298, 313, 323, 333, and 343 K, and the fitted and experimental data are presented in Fig. 6(A). The obtained data distinctly show that with growth in temperature the rate of sorption also rises. The observed temperature dependence in the uptake of Co(II) ions suggests that it is an endothermic reaction, as higher temperatures are conducive to accelerating the reaction rate.

Adsorption thermodynamics

The universal gas constant serves a crucial function in the thermodynamic assessment of the uptake process. The temperature of the adsorption experiments is denoted by T (K). In this context, 'temperature' refers to the measurement in kelvins (K) and the integration of the universal gas constant (8.314 J mol^{-1} K^{-1}).

For a comprehensive thermodynamic analysis, the enthalpy (ΔH) and entropy (ΔS) variations associated with the uptake method are calculated. This is achieved by examining the relationship between log K_d and against $1/T$, as depicted in the plot. From the plot, a slope of -493.5 and an intersection (or y-intercept) of 4.3838 are obtained, along with a significant correlation coefficient ($R^2 = 0.9846$), as illustrated in Fig 6(B). These parameters are instrumental in considering the thermodynamics of the sorption process, providing insight into the heat exchange and disorder changes associated with the sorption of Co(II) ions.

The thermodynamic factors associated with the sorption of Co(II) ions onto PST-SA are concisely tabulated in Table 4. The values recorded for $\Delta G°$, ΔS, and $\Delta H°$ provide substantial evidence regarding the nature of the uptake process. Specifically, the negative value $\Delta G°$ across all temperature ranges underscores the spontaneous nature of the sorption of Co(II) ions. Conversely, the positive value of $\Delta H°$ as detailed in Table 4 corroborates that the sorption of Co(II) ions onto PST-SA is an endothermic process. Furthermore, the positive value of $\Delta S°$ implies a rise in randomness at the solid–solution interface through the sorption process, highlighting randomness or disordered state in the system under consideration.[69,70]

Influence of selectivity for foreign metal ions

The sorption characteristics of Co(II) were explored in multicomponent solutions with varying concentrations (10–250 mg L^{-1}), including nickel, iron, copper, and lithium. The data, shown in (Fig. 7), show that the selectivity of PST-SA is minimally affected by the presence of high concentrations of Cu(II) and Ni(II). However, it is significantly impacted by the occurrence of iron ions and remains unaffected by the existence of Li(I). This observed behavior may be attributed to the PST-SA adsorbent's ability to adsorb foreign cations through an anion-exchange mechanism. The PVC-derived material possesses both an acidic sulfo group and a basic amino group, implying that the polyampholyte can bind non-ferrous and heavy metal ions through chelation and ion exchange. The coordination of metal ions to the amino group via the nitrogen's unpaired electron occurs through ion exchange with the sulfo group in the polyampholyte.

The efficiency and selectivity of PST-SA in capturing Co^{2+} ions depend on the separation factor parameter, denoted by SF*. Analysis of the results presented in Table 5 reveals that under the optimal conditions PST-SA effectively adsorbs Co^{2+} ions with a satisfactory SF* compared to other foreign ions. However, it was noted that while a high SF could be achieved with cations of metal such as Li$^+$, the presence of heavy metals like Cu^{2+}, Ni^{2+}, and Fe^{2+} could slightly impact the adsorption of Co^{2+} ions. This is because these heavy metals may co-adsorb simultaneously with Co^{2+} ions, resulting in different separation factor values.

Elution and regeneration studies

To explore the recovery of Co(II) from PST-SA, desorption assays were conducted using various eluents. Different 0.5 mol L^{-1} acid solutions, namely HCl, H$_2$SO$_4$, EDTA, and HNO$_3$, were employed as eluents. Additionally, the potential elution of Co(II) ions from sorbents when exposed to deionized water was examined as a
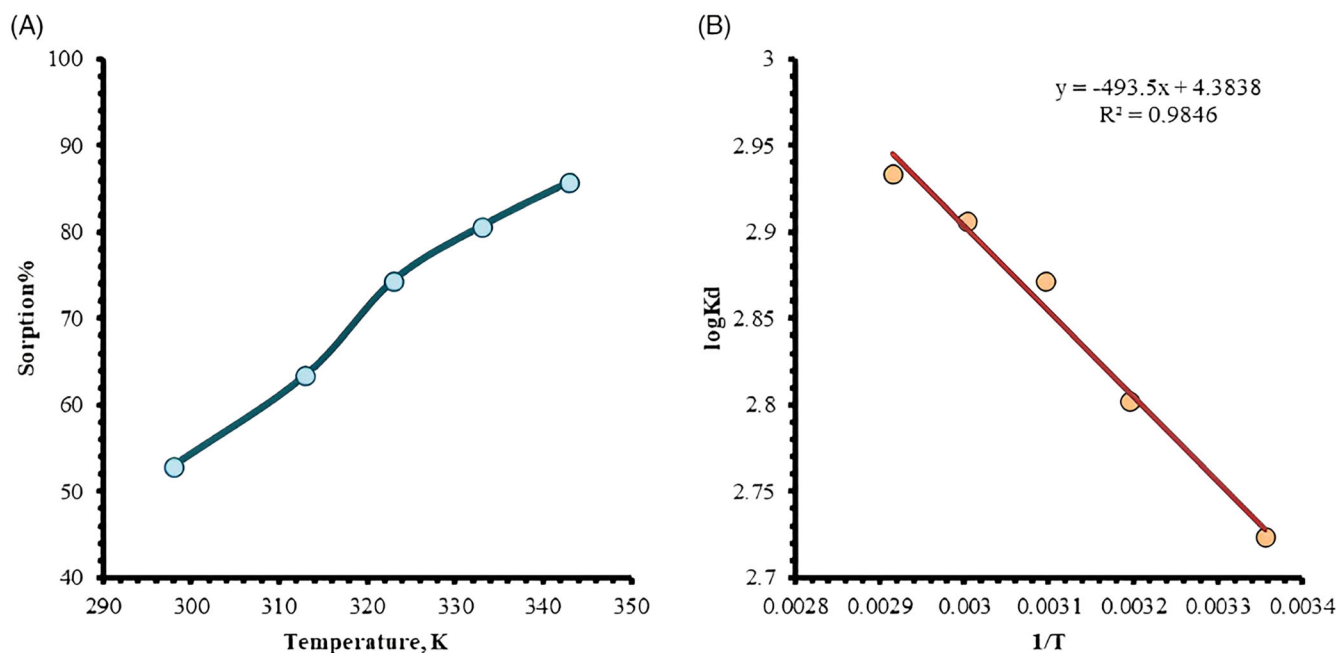
(A)

(B)

$y = -493.5x + 4.3838$
$R^2 = 0.9846$

Figure 6. (A) Temperature effect on the sorption of Co(II) on PST-SA. (B) Plot of log K_d versus $1/T$ of adsorption of Co(II) using PST-SA.

Table 4. Thermodynamic parameters for Co(II) ion uptake by PST-SA at various temperatures

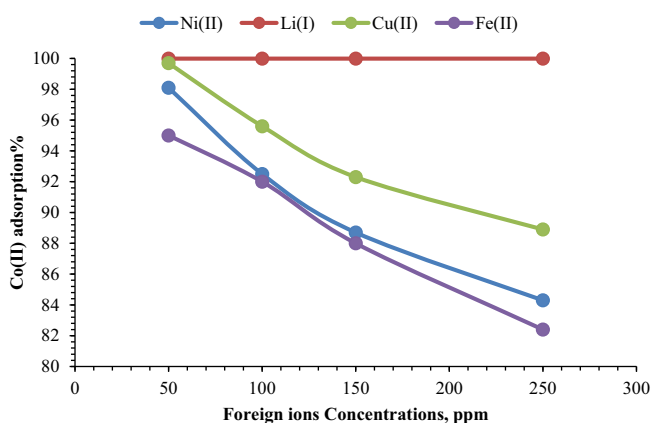| $\Delta H°$ (kJ mol^{-1})	$\Delta S°$ (J mol^{-1} K^{-1})	$\Delta G°$ (kJ mol^{-1})				
		298 K	313 K	323 K	333 K	343 K
9.45	83.94	−25.01	−26.26	−27.1	−27.94	−28.78

Figure 7. Influence of foreign ions on the uptake effectiveness of Co(II) using PST-SA as an adsorbent.

control. As depicted in Fig. 8(A), 0.5 mol L^{-1} HCl solution proved to be the most effective in recovering Co(II) from PST-SA (>84%), followed by solutions of, EDTA, HNO$_3$, and H$_2$SO$_4$, each with a concentration of 0.5 mol L^{-1}. In Fig. 8(A) it is evident that HCl is the most efficient eluent, recovering 84.64% of loaded Co(II). Subsequently, the influence of altered concentrations of HCl on the recovery of Co(II) was explored between 0.1 and 2 mol L^{-1} (Fig. 8(B)). The data illustrate that 1.5 mol L^{-1} HCl is able to recover 90.4% of the loaded Co(II). Finally, the impact of

desorption time was considered in the range 5–90 min, and the obtained data in Fig. 8(C) demonstrate that 60 min was sufficient for recovering almost all Co(II) from the loaded PST-SA. Specifically, the data show that a 60 min desorption time can achieve a recovery rate of >99% for loaded Co(II).

Recovery of PST-SA for uptake of Co(II) ions

The potential for recovering PST-SA following Co(II) adsorption, thereby allowing for recycling and cost reduction, is a critical aspect for the efficiency of the technology. The reusability of PST-SA was investigated through eight successive adsorption–desorption cycles. Figure 8(D) illustrates how the sorption/desorption capacity of Co(II) ions changes with increasing number of cycles. Based on the findings, PST-SA demonstrates promising recyclability. It can be recycled five times with over 97% efficiency, twice with over 95% efficiency, and twice with over 90% efficiency while maintaining optimal adsorption and desorption conditions. The findings imply that PST-SA demonstrates promising potential as a reusable adsorbent for the treatment of Co(II) in practical, real-world applications, indicating its efficacy and sustainability in environmental remediation efforts. The cost-effectiveness of PST-SA further enhances its potential as a viable adsorbent for Co(II) in practical scenarios.

Furthermore, the adsorption capability of PST-SA was compared to that of other alternative adsorbents, as shown in Table 6. Since PST-SA exhibited superior adsorption capacity compared to the majority of the adsorbents, it could be a favorable choice for the dispersion of cobalt ions.

APPLICATIONS

Leaching process of lithium batteries

In this study, the systematic process of collecting and preparing used LIBs for recycling has been meticulously outlined. The

Table 5. The impact of foreign ions on Co^{2+} ion extraction using PST-SA

Co-ion	Feed solution (mg L^{-1})	Raffinate (mg L^{-1})	SF*
Co^{2+}	250	—	—
Li^+	250	250	62 250
Ni^{2+}	250	210.75	1338.71
Cu^{2+}	250	222.25	1995.19
Fe^{2+}	250	206	1169.014

process begins with the careful acquisition of batteries from laptops equipped with $LiCoO_2$ (ICR) cathodes, obtained from the secondary market for IT devices as well as from repair shops. Prioritizing safety, a 24 h immersion in an electrolyte solution (NaCl 5%, w/v) was implemented to mitigate the risk of short circuits.[78] Thorough cleaning using distilled water and subsequent drying at 90 °C for a period of 20 h ensured the removal of contaminants.

The manual opening of cells by cross-cutting through the metal cap followed, facilitating the subsequent separation of components. The contents, including both plastic and sheets of aluminum housing the cathodes, and sheets of copper containing the anodes, were meticulously sorted. The cathodic active material, now in powdered form, underwent a controlled heating process between 250 and 300 °C for 30 min to extract it from the aluminum sheets. This recovered powder then underwent further refinement through milling, achieving a mesh size of less than 200 μm, and meticulous sieving. Each step in this comprehensive
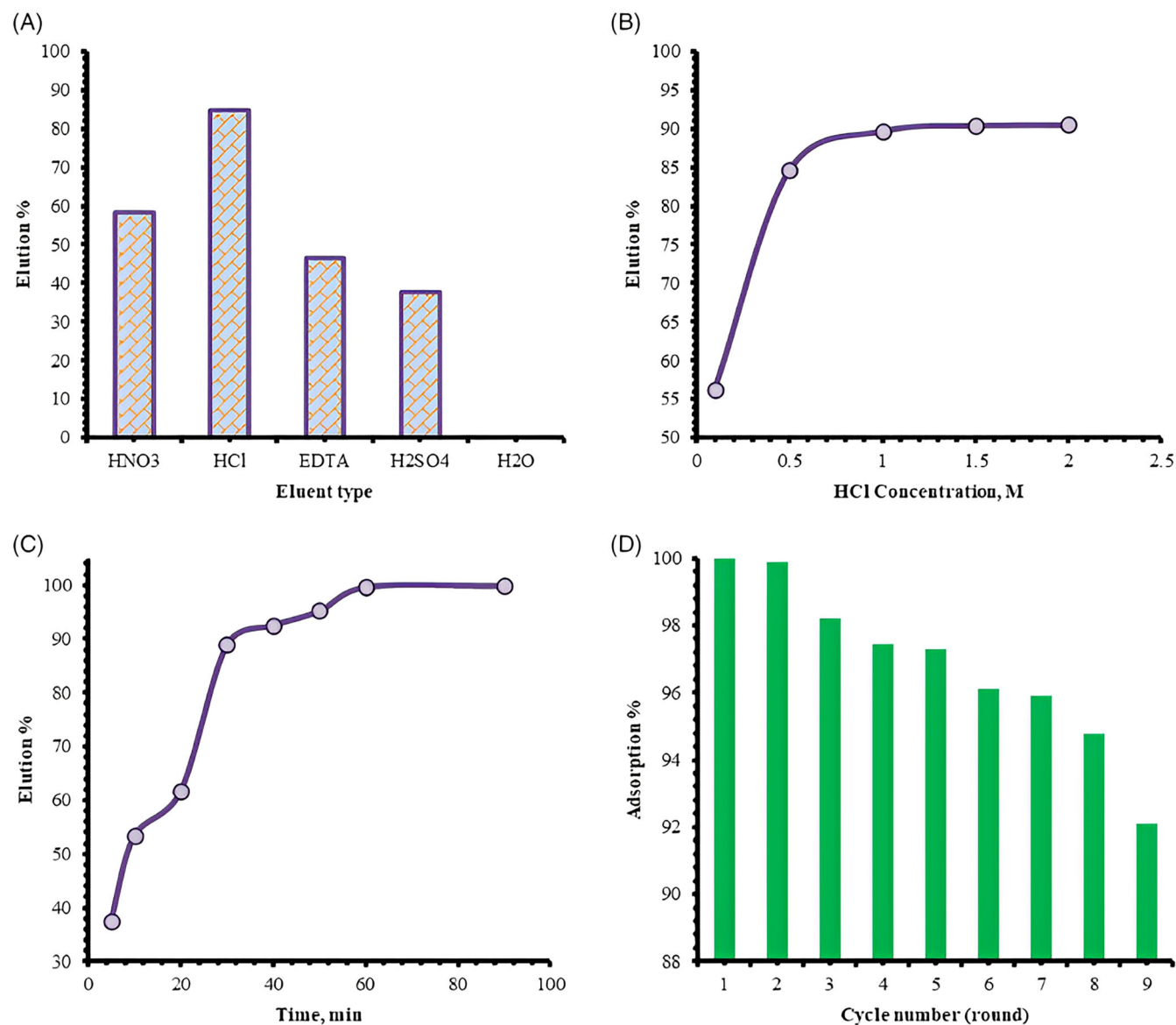

Figure 8. (A) Elution of Co(II) from pregnant PST-SA surface with varies eluting agents, (B) at different HCl concentrations, (C) at changed times. (D) Recycling of PST-SA for the sorption of Co(II) ions.

process was critical, laying the foundation for the successful recycling and reuse of valuable components, particularly cathodes, which potentially contain valuable metals like lithium and cobalt.

Table 6. Adsorbents for Co(II) ion removal: a comparative study

Adsorbent	Adsorption capacity (mg g^{-1})	Reference
Amination graphene oxide nanocomposite	116.4	71
Co(II)-imprinted polymer	181.7	72
Iron/graphene oxide	134.3	73
UiO-66-Schiff base	256	74
Ligand immobilized mesoporous silica	170.2	75
Biogenic glutamic acid-based resin	137	76
MIL-101-triglycine	232.6	77
PST-SA	270.27	This study

The detailed approach exemplifies the commitment to sustainable practices in the reuse of LIBs (Table 6).

Leaching experiments were conducted with 1.5 mol L^{-1} H$_2$SO$_4$, a temperature set at 60 °C, a duration of 60 min, a solid–liquid ratio of 40 g L^{-1}, and a hydrogen peroxide concentration of 15%, providing the highest dissolution efficiencies for working metal values as lithium and cobalt. Cobalt is leached with H$_2$SO$_4$ as hydrogen peroxide reduces it from Co^{3+} to Co^{2+}, with Co^{2+} having enhanced stability compared to Co^{+3}. Both lithium and cobalt are dissolute even at the lowest H$_2$SO$_4$ concentration. The dissolution progression of LiCoO$_2$ in H$_2$SO$_4$ solution can be represented by Eqn (16).[79]

$$2LiCoO_2(s) + 3H_2SO_4(aq) + H_2O_2(aq)$$
$$\rightarrow 2CoSO_4(aq) + Li_2SO_4(aq) + 4H_2O(g) + O_2(g) \tag{16}$$
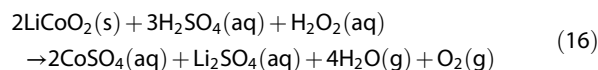
The leaching procedure encompassed a time duration of 180 min. An Lafil 400 (Taiwan) vacuum filtration system was utilized to disperse the leach solution from the insoluble residues. During this process, Whatman (United States) grade GF/B filter paper, measuring 12.5 cm, was employed for effective filtration.

Table 7. Chemical characterization of the starting cathode material for leaching

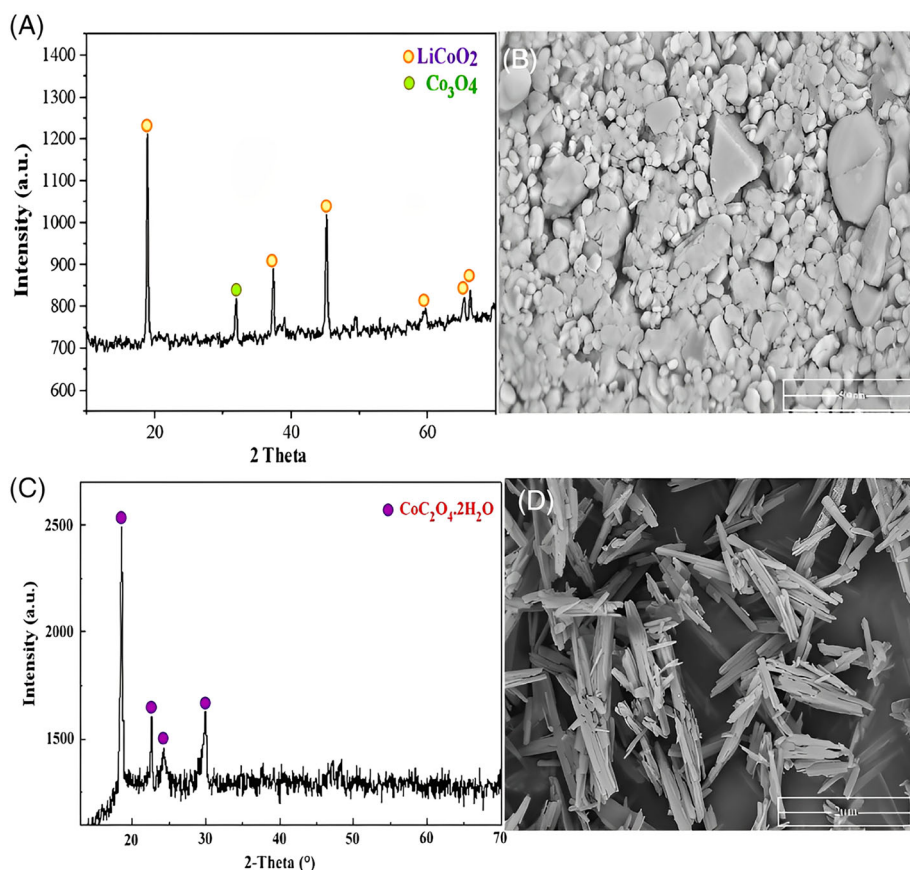| Metal element	Li	Co	Al	Mn
Content (wt%)	5.79	47.86	0.05	0.02

Figure 9. (A) SEM images of cathodic material LiCoO$_2$ and (B) XRD analysis of cathode electrode material.
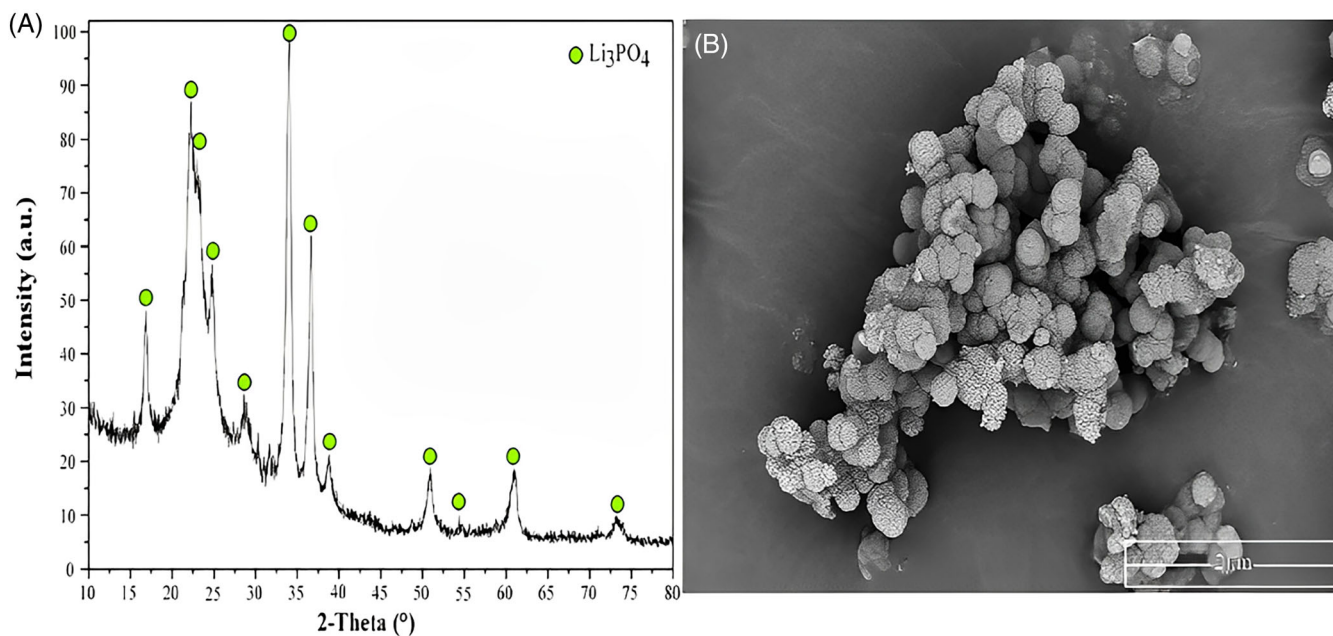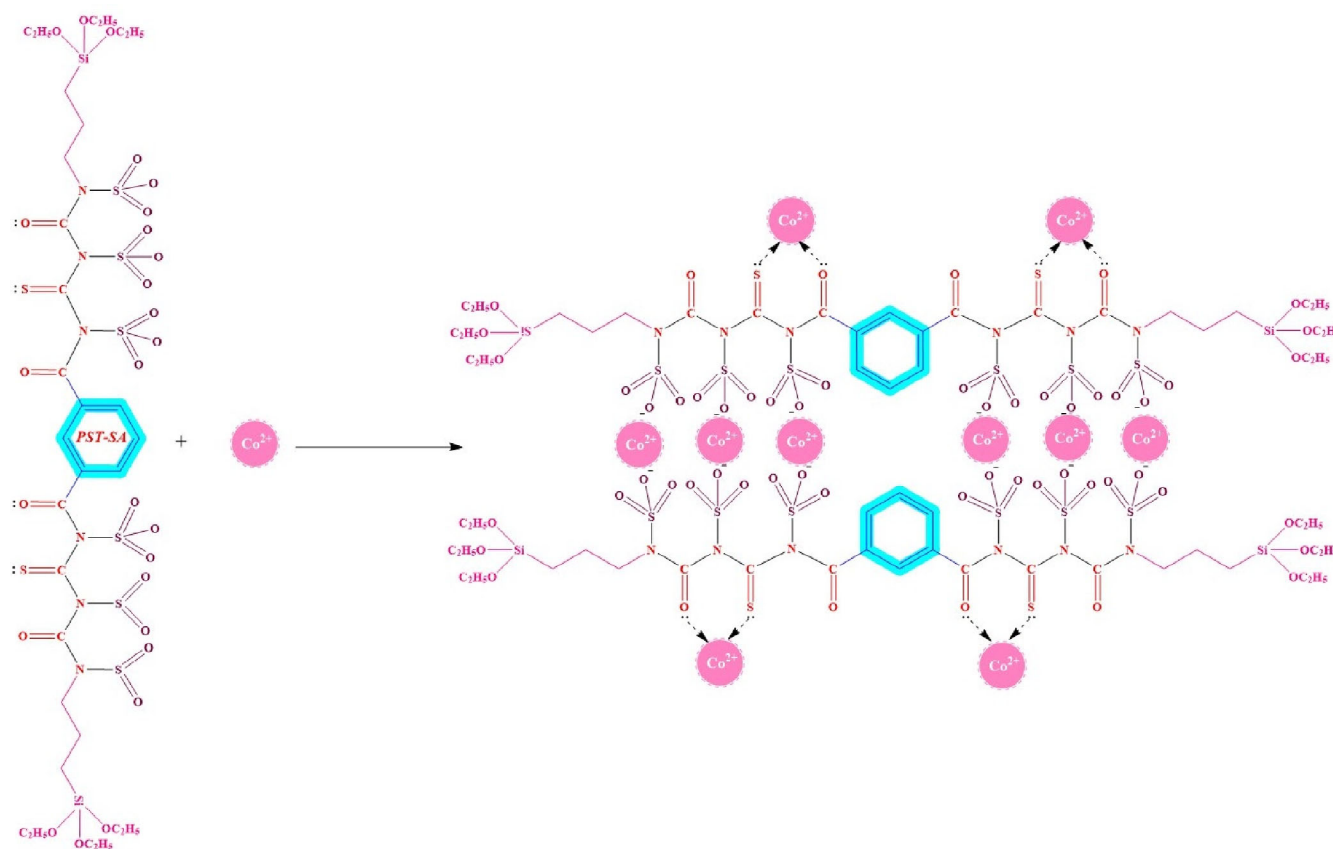
Figure 10. (A) XRD and (B) SEM of the precipitated lithium phosphate (Li$_3$PO$_4$).

**Scheme 2.** Mechanism of reaction between Co(II) and PST-SA.

The liquid samples derived from the leaching process underwent analysis using ICP-OES to scrutinize the metal content (Table 7), with a specific focus on cobalt and lithium. The objective of this analysis was to discern the pivotal factors governing the leaching process.

X-ray diffraction (XRD) investigation of the black cathodic material (Fig. 9(A)) indicated that lithium and cobalt in the form of LiCoO$_2$ were the primary constituents of the cathode's active material. LiCoO$_2$ exhibited the strongest diffraction lines at 19° and 46°. Scanning electron micrography (SEM) of cathode LiCoO$_2$

powders from used LIBs (shown in Fig. 9(B)) revealed uneven morphologies and apparent larger agglomerates. The repeated charging and discharging processes contributed to standardization in particle size. Therefore, $LiCoO_2$ powders extracted from spent LIBs are not suitable for direct use as active materials in cathodes without first being subjected to appropriate recovery and recycling treatments.

Ten grams of the black cathodic powder underwent a leaching process using 250 mL H_2SO_4 (1.5 mol L^{-1}) in the presence of H_2O_2 (15%) for 60 min at 60 °C. Following leaching, the leach liquor was filtered, and the concentrations of cobalt (Co(II)) and lithium were investigated using ICP-OES. The analysis revealed a concentration of 5327 ppm for Co(II) and 1089 ppm for lithium.

Moving on to the second step, the optimal parameters established using PST-SA adsorbent for Co(II) adsorption from the leach liquor were applied. One gram of PST-SA was dispersed in 0.25 L of the waste battery cathode leach liquor, and the liquor pH was controlled to a value of 8 using either 1 mol L^{-1} ammonia or 1 mol L^{-1} H_2SO_4. The blend was stirred for 40 min at a temperature of 70 °C. The leaching efficiency surpassed 96% of the Co(II) content. The Co(II)-loaded PST-SA then underwent an elution process using 1.5 mol L^{-1} HCl with stirring for 1 h at ambient temperature. The obtained solution underwent precipitation using ammonium oxalate, with the liquor pH adjusted to 1.5, and stirring at 300 rpm for 1 h at 75 °C. Cobalt recovery using ammonium oxalate was proposed, and the solid product was cleaned, dried, and analyzed using EDAX and SEM.

$$Li^+_{(aq)} + Co^{2+}_{(aq)} + (NH_4)_2C_2O_{4(aq)} \rightarrow CoC_2O_{4(s)} + Li^+_{(aq)} + 2NH^+_{4(aq)} \tag{17}$$
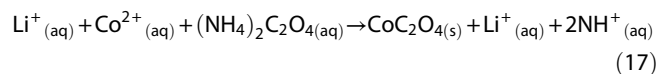
The classification outcomes for CoC_2O_4 during the recovery stages are illustrated in Fig. 9, showcasing both XRD patterns and SEM images of the end product. The XRD analysis confirmed that the final product aligned with the characteristics of pure cobaltous oxalate dihydrate (JCPDS 014-0741). Further examination by SEM revealed that the cobalt oxalate precipitates manifested as agglomerated rod structures, with sizes ranging between 5 and 20 μm. These agglomerates exhibited an acicular crystalline habit and were presented in a layered sub-structure. CoC_2O_4 is pivotal in various applications, including the manufacture of cobalt oxide, cobalt powder catalysts, and $LiCoO_2$.[80,81]

The residual filtrate remaining after the separation of CoC_2O_4 contained all the lithium. This lithium was then exposed to a precipitation process using phosphoric acid. In the second step, a filtrate obtained after separating the CoC_2O_4 in the first stage served as the pregnant leach liquor of lithium, which was used for separating lithium as phosphate using phosphoric acid as a precipitating agent. The pH was raised to 13 and the solution is heated to 70 °C while being agitated at 300 rpm for 60 min. The resulting white precipitate is then filtered and washed several times with distilled water.

A potential chemical reaction for the recovery of lithium from the solution can be represented by the following equation:

$$3Li^+_{(aq)} + H_2PO^-_{4(aq)} + 2NaOH_{(aq)} \rightarrow Li_3PO_{4(s)} + 2Na^+_{(aq)} + 2H_2O \tag{18}$$
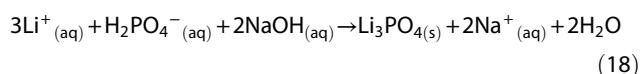
The product was subjected to characterization using micrographs obtained by SEM and XRD. The XRD patterns of the resulting white lithium phosphate precipitate closely matched those of

Li_3PO_4 (JCPDS 015-0760). Additional examination using EDAX patterns reveals that the lithium phosphate particles possess an olivine structure, with a diagonal length ranging from 1 to 2 μm (refer to Fig. 10).

For instance, Li_3PO_4 is employed in the manufacture of dental supplies, and lithium iron phosphate cathode batteries, catalysts underscoring its versatility and significance as a catalyst across various sectors. CoC_2O_4 is employed in the production of a variety of cobalt-based products, excluding powder, catalysts, cobalt oxide, and lithium cobalt oxide.[80]

Mechanism of interaction between Co(II) and PST-SA

The interaction between Co(II) ions and PST-SA is likely to occur through a chelation mechanism, involving the utilization of lone pairs of electrons from oxygen and sulfur atoms. Alternatively, it may take place via a cation-exchange mechanism, facilitated by the occurrence of sulfonic acid groups, as illustrated in Scheme 2.

CONCLUSIONS

In this research endeavor, the novel adsorbent PST-SA has emerged as a highly effective material for Co(II) ion adsorption, exhibiting its versatility by performing well with both synthetic standard solutions and spent LIBs. The comprehensive characterization process, employing FTIR, BET surface area, TGA, ^{1}H-NMR, ^{13}C-NMR, and GC-MS analyses, provided detailed insights into the structure and properties of PST-SA. Adsorption experiments were conducted using the batch technique, revealing optimal conditions at pH 8, a dosage of 0.08 g for PST-SA, a shaking duration of 60 min, and a temperature of 30 °C. Adsorption experiments yielded impressive results, showcasing an extreme uptake capability of 270.70 mg g^{-1} for cobalt, attesting to the efficacy of PST-SA as an adsorbent. Furthermore, thermodynamic examination illuminated the endothermic and spontaneous nature of the sorption method, contributing to a deeper understanding of the underlying mechanisms. Langmuir and D-R isotherms also recommended that the sorption process is a chemical reaction mechanism between Co(II) and the PST-SA binding sites. Applying these findings to real-world scenarios, particularly with spent LIBs, demonstrated the practical utility of PST-SA. The successful separation of cobaltous oxalate and lithium phosphate in a pure state further underscores the potential of PST-SA in the realm of recycling and resource recovery. Its cost-effectiveness and robust adsorption performance position PST-SA as a hopeful candidate for the effective elimination of cobalt(II) from discarded LIBs, thereby contributing to sustainable practices in materials recovery.

CONFLICT OF INTEREST

The authors declare no conflict of interest.

SUPPORTING INFORMATION

Supporting information may be found in the online version of this article.

REFERENCES

1 Thompson DL, Hartley JM, Lambert SM, Shiref M, Harper GDJ, Kendrick E *et al.*, The importance of design in lithium-ion battery recycling – a critical review. *Green Chem* **22**:7585–7603 (2020). https://doi.org/10.1039/D0GC02745F.

2 Michaels KC, The role of critical minerals in clean energy transitions, in Mining and Sustainability Forum of the Americas. Paris, France. (2021) https://www.iea.org/reports/the-role-of-critical-minerals-in-clean-energy-transitions.

3 Blengini G, Latunussa C, Eynard U, Matos C, Georgitzikis K, Pavel C *et al.*, Study on the EU's list of Critical Raw Materials. Final Report, 2020 (2020). https://doi.org/10.2873/11619, https://op.europa.eu/en/publication-detail/-/publication/88f08133-f895-11ea-991b-01aa75ed71a1/language-en.

4 Alves Dias P, Blagoeva D, Pavel C and Arvanitidis N, *Cobalt:demand-supply balances in the transition to electric mobility*, Vol. **JRC112285**. *Publications Office of the European Union*, Luxembourg (2018). https://doi.org/10.2760/97710.

5 Peng C, Hamuyuni J, Wilson BP and Lundstrom M, Selective reductive leaching of cobalt and lithium from industrially crushed waste Li-ion batteries in sulfuric acid system. *Waste Manag* **76**:582–590 (2018). https://doi.org/10.1016/j.wasman.2018.02.052.

6 Gaines L, Lithium-ion battery recycling processes: research towards a sustainable course. *Sustain Mater Technol* **17**:e00068 (2018). https://doi.org/10.1016/j.susmat.2018.e00068.

7 Yin W, Wu Z, Tian W, Chen Y, Xiang W, Feng G *et al.*, Enhanced constraint and catalyzed conversion of lithium polysulfides: via composite oxides from spent layered cathodes. *J Mater Chem* **A7**:17867–17875 (2019). https://doi.org/10.1039/c9ta06116a.

8 Zhang X, Tang Y, Zhang F and Lee C, A novel aluminum-graphite dual-ion battery. *Adv Energy Mater* **6**:1502588 (2016). https://doi.org/10.1002/aenm.201502588.

9 Wang M, Jiang C, Zhang S, Song X, Tang Y and Cheng H, Reversible calcium alloying enables a practical room-temperature rechargeable calcium-ion battery with a high discharge voltage. *Nat Chem* **10**:667–672 (2018). https://doi.org/10.1038/s41557-018-0045-4.

10 Perez JPH, Folens K, Leus K, Vanhaecke F, Van Der Voort P and Du Laing G, Progress in hydrometallurgical technologies to recover critical raw materials and precious metals from low-concentrated streams. *Resour Conserv Recycl* **142**:177–188 (2019). https://doi.org/10.1016/j.resconrec.2018.11.029.

11 Botelho Junior AB, Jiménez Correa MM, Espinosa DCR, Dreisinger D and Tenório JAS, Recovery of Cu(II) from nickel laterite leach using pre-reduction and chelating resin extraction: batch and continuous experiments. *Can J Chem Eng* **97**:924–929 (2019). https://doi.org/10.1002/cjce.23306.

12 Perez ID, Botelho Junior AB, Aliprandini P and Espinosa DCR, Copper recovery from nickel laterite with high-iron content: a continuous process from mining waste. *Can J Chem Eng* **98**:957–968 (2020). https://doi.org/10.1002/cjce.23667.

13 Liu W, Zhao Q, Yu H, Wang H, Huang S, Zhou L *et al.*, Metallic particles-induced surface reconstruction enabling highly durable zinc metal anode. *Adv Funct Mater* **33**:2302661 (2023). https://doi.org/10.1002/adfm.202302661.

14 Botelho Junior AB, Vicente ADA, Espinosa DCR and Tenório JAS, Effect of iron oxidation state for copper recovery from nickel laterite leach solution using chelating resin. *Sep Sci Technol* **55**:788–798 (2020). https://doi.org/10.1080/01496395.2019.1574828.

15 Torkaman R, Asadollahzadeh M, Torab-Mostaedi M and Ghanadi Maragheh M, Recovery of cobalt from spent lithium-ion batteries by using acidic and basic extractants in solvent extraction process. *Sep Purif Technol* **186**:318–325 (2017). https://doi.org/10.1016/j.seppur.2017.06.023.

16 Kumar A, Holuszko M and Espinosa DCR, E-waste: an overview on generation, collection, legislation and recycling practices. *Resour Conserv Recycl* **122**:32–42 (2017). https://doi.org/10.1016/j.resconrec.2017.01.018.

17 Mauger A and Julien C, Critical review on lithium-ion batteries: are they safe? Sustainable? *Ionics* **23**:1933–1947 (2017). https://doi.org/10.1007/s11581-017-2177-8.

18 Mu S, Liu Q, Kidkhunthod P, Zhou X, Wang W and Tang Y, Molecular grafting towards high-fraction active nanodots implanted in N-doped carbon for sodium dual-ion batteries. *Natl Sci Rev* **8**:nwaa178-nwaa190 (2020). https://doi.org/10.1093/nsr/nwaa178.

19 Huang Z, Luo P, Jia S, Zheng H and Lyu Z, A sulfur-doped carbon-enhanced Na3V2(PO4)3 nanocomposite for sodium-ion storage. *J Phys Chem Solids* **167**:110746 (2022). https://doi.org/10.1016/j.jpcs.2022.110746.

20 Winslow KM, Laux SJ and Townsend TG, A review on the growing concern and potential management strategies of waste lithium-ion batteries. *Resour Conserv Recycl* **129**:263–277 (2018). https://doi.org/10.1016/j.resconrec.2017.11.001.

21 Mossali E, Picone N, Gentilini L, Rodrìguez O, Perez JM and Colledani M, Lithium-ion batteries towards circular economy: a literature review of opportunities and issues of recycling treatments. *J Environ Manag* **264**:110500 (2020). https://doi.org/10.1016/j.jenvman.2020.110500.

22 Boyden A, Soo VK and Doolan M, The environmental impacts of recycling portable Lithium-ion batteries. *Procedia CIRP* **48**:188–193 (2016). https://doi.org/10.1016/j.procir.2016.03.100.

23 Julien C, Mauger A, Vijh A and Zaghib K, Lithium batteries: science and technology, in *Lithium Batteries*. Sorbonne Universités, UPMC Univ, Paris, France, pp. 29–68 (2016). https://doi.org/10.1007/978-3-319-19108-9.

24 Ma J, Qiu Y, Zhao J, Ouyang X, Zhao Y, Weng L *et al.*, Effect of agricultural organic inputs on Nanoplastics transport in saturated goethite-coated porous media: particle size selectivity and role of dissolved organic matter. *Environ Sci Technol* **56**:3524–3534 (2022). https://doi.org/10.1021/acs.est.1c07574.

25 Cayumil R, Khanna R, Rajarao R, Mukherjee P and Sahajwalla V, Concentration of precious metals during their recovery from electronic waste. *Waste Manag* **57**:121–130 (2016). https://doi.org/10.1016/j.wasman.2015.12.004.

26 Assefi M, Maroufi S, Yamauchi Y and Sahajwalla V, Pyrometallurgical recycling of Li-ion, Ni–Cd and Ni–MH batteries: a minireview. *Curr Opin Green Sustain Chem* **24**:26–31 (2020). https://doi.org/10.1016/j.cogsc.2020.01.005.

27 Huang Z, Luo P, Wu Q and Zheng H, Constructing one-dimensional mesoporous carbon nanofibers loaded with NaTi$_2$(PO$_4$)$_3$ nanodots as novel anodes for sodium energy storage. *J Phys Chem Solids* **161**:110479 (2022). https://doi.org/10.1016/j.jpcs.2021.110479.

28 Gao J, Liu J, Yang H, Liu H, Zeng G and Huang B, Anisotropic medium sensing controlled by bound states in the continuum in polarization-independent metasurfaces. *Opt Express* **31**:44703–44719 (2023). https://doi.org/10.1364/OE.509673.

29 Chen X, Luo C, Zhang J, Kong J and Zhou T, Sustainable recovery of metals from spent lithium-ion batteries: a green process. *ACS Sustain Chem Eng* **3**:3104–3113 (2015). https://doi.org/10.1021/acssuschemeng.5b01000.

30 Lv W, Wang Z, Cao H, Sun Y, Zhang Y and Sun Z, A critical review and analysis on the recycling of spent lithium-ion batteries. *ACS Sustain Chem Eng* **6**:1504–1521 (2018). https://doi.org/10.1021/acssuschemeng.7b03811.

31 Wang W, Zhang Y, Liu X and Xu S, A simplified process for recovery of Li and Co from spent LiCoO$_2$ cathode using Al foil as the in-situ reductant. *ACS Sustain Chem Eng* **7**:12222–12230 (2019). https://doi.org/10.1021/acssuschemeng.9b01564.

32 Zhang Y, Gao H, Wang J, Chi Q, Zhang T, Zhang C *et al.*, PEO/-Li$_{1.25}$Al$_{0.25}$Zr$_{1.75}$(PO$_4$)$_3$ composite solid electrolytes for high-rate and ultra-stable all-solid-state lithium metal batteries with impregnated cathode modification. *Inorg Chem Front* **11**: 1289-1300 (2024). DOI.10.1039/D3QI02407E.

33 Wang Z, Fu W, Hu L, Zhao M, Guo T, Hrynsphan D *et al.*, Improvement of electron transfer efficiency during denitrification process by Fe-Pd/multi-walled carbon nanotubes: possessed redox characteristics and secreted endogenous electron mediator. *Sci Total Environ* **781**: 146686 (2021). https://doi.org/10.1016/j.scitotenv.2021.146686.

34 Sloop S, Crandon L, Allen M, Koetje K, Reed L, Gaines L *et al.*, A direct recycling case study from a lithium-ion battery recall. *Sustain Mater Technol* **25**:e00152 (2020). https://doi.org/10.1016/j.susmat.2020.e00152.

35 Liu F, Peng C, Porvali A, Wang Z, Wilson BP and Lundstrom M, Synergistic recovery of valuable metals from spent nickel–metal hydride batteries and lithium-ion batteries. *ACS Sustain Chem Eng* **7**:16103–16111 (2019). https://doi.org/10.1021/acssuschemeng.9b02863.

36 He LP, Sun SY, Mu YY, Song XF and Yu JG, Recovery of lithium, nickel, cobalt, and manganese from spent lithium-ion batteries using L-tartaric acid as a leachant. *ACS Sustain Chem Eng* **5**:714–721 (2017).

37 Li Q, Wang H, Yu H, Fu M, Liu W, Zhao Q *et al.*, Engineering an ultrathin and hydrophobic composite zinc anode with 24 μm thickness for

high-performance Zn batteries. *Adv Funct Mater* **33**:2303466 (2023). DOI.10.1002/adfm.202303466.

38 Iqbal A, Jan MR and Shah J, Recovery of cadmium, lead, and nickel from leach solutions of waste electrical and electronic equipment using activated carbon modified with 1-(2-pyridylazo)-2-naphthol. *Hydrometallurgy* **201**:105570 (2021). https://doi.org/10.1016/j.hydromet.2021.105570.

39 Kyzas GZ, Deliyanni EA and Matis KA, Activated carbons produced by pyrolysis of waste potato peels: cobalt ions removal by adsorption. *Colloids Surf A Physicochem Eng Asp* **490**:74–83 (2016). https://doi.org/10.1016/j.colsurfa.2015.11.038.

40 Jimenez-Reyes M and Solache-Ríos M, Chemical behavior of cobalt and cesium in the presence of inorganic components of a semiarid soil using water of nuclear purity. *Process Saf Environ Prot* **102**:288–293 (2016). https://doi.org/10.1016/j.psep.2016.04.003.

41 Dehghani MH, Yetilmezsoy K, Salari M, Heidarinejad Z and Yousefi M, Sillanpӓӓ, M, adsorptive removal of cobalt(II) from aqueous solutions € using multi-walled carbon nanotubes and g-alumina as novel adsorbents: modelling and optimization based on response surface methodology and artificial neural network. *J Mol Liq* **299**:112154 (2020). https://doi.org/10.1016/j.molliq.2019.112154.

42 Lu L, Wu W, Gao Y, Pan C, Yu X, Zhang C *et al.*, Study on current discrepancy and redistribution of HTS non-insulation closed-loop coils during charging/discharging and subsequent transient process toward steady-state operation. *Supercond Sci Technol* **35**:95001 (2022). https://doi.org/10.1088/1361-6668/ac7dfe.

43 Yang X, Liu K, Han X, Xu J, Bian M, Zheng D *et al.*, Transformation of waste battery cathode material LiMn2O4 into efficient ultra-low temperature NH3-SCR catalyst: proton exchange synergistic vanadium modification. *J Hazard Mater* **459**:132209 (2023). DOI.10.1016/j.jhazmat.2023.132209.

44 Swelam AA, Awad MB, Salem AMA and El-Feky AS, An economically viable method for the removal of cobalt ions from aqueous solution using raw and modified rice straw. *HBRC J* **14**:255–263 (2018). https://doi.org/10.1016/j.hbrcj.2016.10.001.

45 Peres EC, Cunha JM, Dortzbacher GF, Pavan FA, Lima EC, Foletto EL *et al.*, Treatment of leachates containing cobalt by adsorption on spirulina sp. and activated charcoal. *J Environ Chem Eng* **6**:677–685 (2018). https://doi.org/10.1016/j.jece.2017.12.060.

46 Rzetala MA, Cobalt and vanadium in bottom sediments of anthropogenic lakes in the Silesian upland (southern Poland), in *International Multidisciplinary Scientific GeoConference: SGEM: Surveying Geology & Mining Ecology and Management*. Hamilton, New Zealand, pp. 9–176 (2016).

47 Rocío Montes de Oca-Palma, Marcos Solache-Ríos, Melania Jiménez-Reyes, José Juan García-Sánchez, Perla Tatiana Almazán-Sánchez, adsorption of cobalt by using inorganic components of sediment samples from water bodies. *Int J Sediment Res* **36**:524–531 (2021). https://doi.org/10.1016/j.ijsrc.2020.11.003.

48 Asefa T, MacLachlan MJ, Coombs N and Ozin GA, Periodic mesoporous organosilicas with organic groups inside the channel walls. *Nature* **402**:867–871 (1999). https://doi.org/10.1038/47229.

49 Lim MH, Blanford CF and Stein A, Synthesis and characterization of a reactive vinyl-functionalized MCM-41: probing the internal pore structure by a Bromination reaction. *J Am Chem Soc* **119**:4090–4091 (1997). https://doi.org/10.1021/ja9638824.

50 Lim MH, Blanford CF and Stein A, Synthesis of ordered microporous silicates with organosulfur surface groups and their applications as solid acid catalysts. *Chem Mater* **10**:467–470 (1998). https://doi.org/10.1021/cm970713p.

51 Ibrahium HA, Awwad NS, Gado MA, Hassanin MA, Nayl AA and Atia BM, Physico-chemical aspects on uranium and molybdenum extraction from aqueous solution by synthesized Phosphinimine derivative chelating agent. *J Inorg Organomet Polym* **32**:3640–3657 (2022). https://doi.org/10.1007/s10904-022-02374-1.

52 Nakajima K and Hara M, Amorphous carbon with SO3H groups as a solid Brønsted acid catalyst. *ACS Catal* **2**:1296–1304 (2012). https://doi.org/10.1021/cs300103k.

53 Madhurambal G, Ravindran B, Mariappan M and Mojumdar SC, Growth and characterization of tris thiourea chromium(III) sulphate. *J Therm Anal Calorim* **108**:905–910 (2012). https://doi.org/10.1007/s10973-012-2360-0.

54 Lin-Vien D, Colthup NB, Fateley WG and Grasselli JG, CHAPTER 10 – compounds containing –NH2, –NHR, and –NR2 groups, in *The Handbook of Infrared and Raman Characteristic Frequencies of Organic Molecules*. Academic Press, San Diego, pp. 155–178 (1991).

55 Van der Voort P, Ravikovitch PI, de Jong KP, Neimark AV, Janssen AH, Benjelloun M *et al.*, Plugged hexagonal templated silica: a unique micro- and mesoporous composite material with internal silica nanocapsules. *Chem Commun* **9**:1010–1011 (2002). https://doi.org/10.1039/B201424F.

56 Geszke-Moritz M and Moritz M, Modeling of boldine alkaloid adsorption onto pure and propyl-sulfonic acid-modified mesoporous silicas, A comparative study. *Mater Sci Eng* **C69**:815–830 (2016). https://doi.org/10.1016/j.msec.2016.07.055.

57 Nasresfahani Z, Kassaee MZ and Eidi E, Homopiperazine sulfamic acid functionalized mesoporous silica nanoparticles (MSNs-HPZ-SO3H) as an efficient catalyst for one-pot synthesis of 1-amidoalkyl-2-naphthols. *New J Chem* **40**:4720–4726 (2016). https://doi.org/10.1039/C5NJ02974K.

58 Valiey E, Dekamin MG and Alirezvani Z, Sulfamic acid pyromellitic diamide-functionalized MCM-41 as a multifunctional hybrid catalyst for melting-assisted solvent-free synthesis of bioactive 3,4-dihydropyrimidin-2-(1H)-ones. *Sci Rep* **11**:1199 (2021). https://doi.org/10.1038/s41598-021-89572-y.

59 Ibrahim AH, Lyu X, Atia BM, Gado MA and ElDeeb AB, Phase transformation mechanism of boiler ash roasted with sodium salt for vanadium extraction. *J Mater Cycles Waste Manag* **25**:86–102 (2023). https://doi.org/10.1007/s10163-022-01512-8.

60 Alluhaybi AA, Alharbi A, Hameed AM, Gouda AA, Hassen FS, El-Gendy HS *et al.*, A novel Triazole Schiff Base derivatives for remediation of chromium contamination from tannery waste water. *Molecules* **27**:5087 (2022). https://doi.org/10.3390/molecules27165087.

61 Ibrahim HA, Atia BM, Awwad NS, Nayl AA, Radwan HA and Gado MA, Efficient preparation of phosphazene chitosan derivatives and its applications for the adsorption of molybdenum from spent hydrodesulfurization catalyst. *J Dispers Sci Technol* **44**:2103–2118 (2023). https://doi.org/10.1080/01932691.2022.2059508.

62 Alharbi A, Gouda AA, Atia BM, Gado MA, Alluhaybi AA and Alkabli J, The role of modified chelating graphene oxide for vanadium separation from its bearing samples. *Russ J Inorg Chem* **67**:560–575 (2022). https://doi.org/10.1134/S0036023622040027.

63 Ibrahium HA, Gado MA, Ali HE, Fathy WM, Atia BM and Awwad NS, Synthesis of chelating N-hydroxyl amine derivative and its application for vanadium separation from Abu Zeneima ferruginous siltstone ore, southwestern Sinai, Egypt. *Int J Environ Anal Chem* **103**:8496–8518 (2023). https://doi.org/10.1080/03067319.2021.1987425.

64 Garoub M and Gado M, Separation of cadmium using a new adsorbent of modified chitosan with pyridine Dicarboxyamide derivative and application in different samples. *Z Anorg Allg Chem* **648**:28–47 (2022). https://doi.org/10.1002/zaac.202100222.

65 Atia BM, Gado MA, Abd El-Magied MO and Elshehy EA, Highly efficient extraction of uranyl ions from aqueous solutions using multi-chelators functionalized graphene oxide. *Sep Sci Technol* **55**:2746–2757 (2020). https://doi.org/10.1080/01496395.2019.1650769.

66 Dubinin MM, The potential theory of adsorption of gases and vapors for adsorbents with energetically non uniform surfaces. *Chem Rev* **60**:235–241 (1960). https://doi.org/10.1021/cr60204a006.

67 Akar T, Kaynak Z, Ulusoy S, Yuvaci D, Ozsari G and Akar ST, Enhanced biosorption of nickel(II) ions by silica-GelImmobilized waste biomass: biosorption characteristics in batch and dynamic flow mode. *J Hazard Mater* **163**:1134–1141 (2009). https://doi.org/10.1016/j.jhazmat.2008.07.084.

68 Chen AH and Chen SM, Biosorption of azo dyes from aqueous solution by glutaraldehyde-Crosslinked Chitosans. *J Hazard Mater* **172**:1111–1121 (2009). https://doi.org/10.1016/j.jhazmat.2009.07.104.

69 Radwan HA, Faheim AA, El-Sheikh EM, Abd El-Wahab ZH and Gado MA, Optimization of the leaching process for uranium recovery and some associated valuable elements from low-grade uranium ore. *Int J Environ Anal Chem* **103**:5259–5281 (2023). https://doi.org/10.1080/03067319.2021.1936513.

70 Gado M, Rashad M, Kassab W and Badran M, Highly developed surface area Thiosemicarbazide biochar derived from aloe Vera for efficient adsorption of uranium. *Radiochemistry* **63**:353–363 (2021). https://doi.org/10.1134/S1066362221030139.

71 Fang F, Kong L, Huang J, Wu S, Zhang K, Wang X *et al.*, Removal of cobalt ions from aqueous solution by an amination graphene oxide nanocomposite. *J Hazard Mater* **270**:1–10 (2014). https://doi.org/10.1016/j.jhazmat.2014.01.031.

72 Guo WL, Chen R, Liu Y, Meng MJ, Meng XG, Hu ZY *et al.*, Preparation of ion-imprinted mesoporous silica SBA-15 functionalized with

triglycine for selective adsorption of Co(II). *Colloid Surf A* **436**:693–703 (2013). https://doi.org/10.1016/j.colsurfa.2013.08.011.

73 Xing M and Wang J, Nanoscaled zero valent iron/graphene composite as an efficient adsorbent for Co(II) removal from aqueous solution. *J Colloid Interface Sci* **474**:119–128 (2016). https://doi.org/10.1016/j.jcis.2016.04.031.

74 Yuan G, Tian Y, Liu J, Tu H, Liao J, Yang J *et al.*, Schiff base anchored on metal-organic framework for Co(II) removal from aqueous solution. *Chem Eng J* **326**:691–699 (2017). https://doi.org/10.1016/j.cej.2017.06.024.

75 Awual MR, Alharthi NH, Hasan MM, Karim MR, Islam A, Znad H *et al.*, Inorganic-organic based novel nano-conjugate material for effective cobalt(II) ions capturing from wastewater. *Chem Eng J* **324**:130–139 (2017). https://doi.org/10.1016/j.cej.2017.05.026.

76 Jamiu ZA, Saleh TA and Ali SA, Biogenic glutamic acid-based resin: its synthesis and application in the removal of cobalt(II). *J Hazard Mater* **327**:44–54 (2017). https://doi.org/10.1016/j.jhazmat.2016.12.041.

77 Yuan G, Tu H, Li M, Liu J, Zhao C, Liao J *et al.*, Glycine derivative-functionalized metal-organic framework (MOF) materials for Co(II) removal from aqueous solution. *Appl Surf Sci* **466**:903–910 (2019). https://doi.org/10.1016/j.apsusc.2018.10.129.

78 Jha AK, Jha MK, Kumari A, Sahu SK, Kumar V and Pandey BD, Selective separation and recovery of cobalt from leach liquor of discarded Li-ion batteries using thiophosphinic extractant. *Sep Purif Technol* **104**:160–166 (2013). https://doi.org/10.1016/j.seppur.2012.11.024.

79 Sun L and Qiu K, Organic oxalate as leachant and precipitant for the recovery of valuable metals from spent lithium-ion batteries. *Waste Manag* **32**:1575–1582 (2012). https://doi.org/10.1016/j.wasman.2012.03.027.

80 Habashi F, *Handbook of Extractive Metallurgy*. Wiley-VCH, Quebec (1997).

81 Cai X, Li X, You J, Yang F, Shadike Z, Qin S *et al.*, Lithium-mediated ammonia Electrosynthesis with ether-based electrolytes. *J Am Chem Soc* **145**:25716–25725 (2023). https://doi.org/10.1021/jacs.3c08965.